Development of a coupled level set and immersed boundary method for predicting dam break flows

C.H. Yu [a], Tony W.H. Sheu [b,c,d,*]

[a] School of Civil Engineering and Architecture, Xiamen University of Technology, Xiamen, People's Republic of China
[b] Department of Engineering Science and Ocean Engineering, National Taiwan University, No. 1, Sec. 4, Roosevelt Road, Taipei, Taiwan, ROC
[c] Institute of Applied Mathematical Sciences, National Taiwan University, Taiwan, ROC
[d] Center for Advanced Study in Theoretical Sciences, National Taiwan University, Taiwan, ROC

ABSTRACT

Dam-break flow over an immersed stationary object is investigated using a coupled level set (LS)/immersed boundary (IB) method developed in Cartesian grids. This approach adopts an improved interface preserving level set method which includes three solution steps and the differential-based interpolation immersed boundary method to treat fluid–fluid and solid–fluid interfaces, respectively. In the first step of this level set method, the level set function ϕ is advected by a pure advection equation. The intermediate step is performed to obtain a new level set value through a new smoothed Heaviside function. In the final solution step, a mass correction term is added to the re-initialization equation to ensure the new level set is a distance function and to conserve the mass bounded by the interface. For accurately calculating the level set value, the four-point upwinding combined compact difference (UCCD) scheme with three-point boundary combined compact difference scheme is applied to approximate the first-order derivative term shown in the level set equation. For the immersed boundary method, application of the artificial momentum forcing term at points in cells consisting of both fluid and solid allows an imposition of velocity condition to account for the presence of solid object. The incompressible Navier–Stokes solutions are calculated using the projection method. Numerical results show that the coupled LS/IB method can not only predict interface accurately but also preserve the mass conservation excellently for the dam-break flow.

© 2017 Elsevier B.V. All rights reserved.

1. Introduction

Dam-break flows interacting with solid bodies are commonly observed in hydraulics and civil engineering [1,2]. Computational methods developed for simulating dam-break flows in a complex domain can be categorized into three classes: meshless, moving grid, and fixed grid methods. Meshless or meshfree methods such as the smoothed particle hydrodynamics (SPH) [3], moving particle semi-implicit (MPS) [4,5] methods have featured their remarkable flexibilities in handling interface deformation as well as fragmentation. These methods do not require grid structure, thereby alleviating a time consuming and troublesome mesh generation. However, due to the difficulty of coping with the Laplacian operator, application of a meshless method is limited normally to low Reynolds number flow simulation. In moving grid methods, classical body-fitted grid-based methods, which are used to discretize the governing equations in curvilinear coordinates that conform to physical boundaries, involve re-gridding mesh at each time step. It is well known that grid generation requires considerable manpower and computational time. In fixed grid methods [6–8], treatment of fluid–fluid interfaces and solid boundaries need to be taken into account when predicting an interface flow inside which there is a solid body. Solid boundaries and fluid–fluid interfaces may have unrestricted motions across the underlying fixed grid lines. These methods simplify the gridding requirements and have been applied to fixed curvilinear and unstructured grids. In this study, a coupled level set (LS)/immersed boundary (IB) method, which belongs to the fixed grid method, is chosen to simulate incompressible fluid flow over solid bodies of different shapes.

Level set method [9–15] is one of the popular fluid–fluid interface capturing methods. The level set method is a successful approach developed to model two-phase flows, especially for the case with a marked topological change. Given a level set function for the physical interface, both shape and its curvature of this interface can be easily transported and accurately calculated, respectively. Choice of a proper signed distance function for re-shaping level set function and implementation of re-initialization

* Corresponding author at: Department of Engineering Science and Ocean Engineering, National Taiwan University, No. 1, Sec. 4, Roosevelt Road, Taipei, Taiwan, ROC.

E-mail address: twhsheu@ntu.edu.tw (T.W.H. Sheu).

procedure for the purpose of enhancing numerical stability are normally required while applying the level set methods. Level set method applied to predict interface suffers the problems of numerical dissipation and non-conserved mass. Many attempts have been made to cope with these two difficulties. The global mass correction equation [16,17] coupled with the first and second distance functions is used to preserve mass in time. In addition, for improving mass conservation using the level set method, one can also apply the hybrid method such as the coupled level set and volume of fluid (CLSVOF) method [18–21]. The other method known as the particle level set (PLS) method [22,23] combines the advantage of Lagrangian tracking methods owing to their simplicity and the efficiency embedded in level set method. It is also numerically possible to improve mass conservation by using the volume preserving level set method [24,25]. Volume preserving level set method uses high-order upwinding combined compact difference (UCCD) and high-order symplectic Runge–Kutta (SRK) scheme for the approximation of the spatial derivative term and the temporal derivative term shown in the level set equation, respectively. The conservative level set method [26,27] solves a conservative form of the LS advection equation with the high resolution scheme. Then, a re-initialization equation with the artificial compression and viscosity terms is applied to sharpen interface and to avoid small interface thickness. The mass conservation is significantly better for the conservative level set method as compared to the conventional level set method introduced in [9].

For modeling solid boundaries in fluid flow, the immersed boundary (IB) method has become increasingly popular since generation of grids can be greatly simplified when simulating flow problems with complex stationary or moving boundaries. Immersed boundary methods include the continuous and discrete forcing methods [28]. The first class of methods involves adding a forcing term into the continuous governing equations prior to the discretization of the differential equations. Since the constitutive equations can be directly incorporated into the formulation, application of continuous forcing methods can give us a sound physical basis to accurately simulate fluid flow problem with elastic boundary. It is therefore applicable to simulate biological flows rather than to predict flows containing rigid bodies. Another advantage of applying continuous forcing methods roots in the fact that these methods can be formulated independent of the employed spatial discretization. This typical continuous forcing method due firstly to the original work of Peskin [29] was subsequently extended by Goldstein et al. [30]. In the discrete forcing methods, the forcing term is either explicitly or implicitly applied to the discretized Navier–Stokes equations [31–33]. In comparison with the first category of the immersed boundary methods, discrete forcing methods allow adopting a sharper representation of the immersed boundary. More application of IB method can be found in Refs. [34–37].

In this study, a combined LS/IB method will be implemented in Cartesian grid system. The fluid–fluid interface is captured through the use of the currently adopted high-order level set method, the application of the sixth-order accurate symplectic Runge–Kutta scheme, and the sixth-order accurate upwinding combined compact difference scheme. This upwinding combined compact difference scheme is manifested with the minimized phase error, thereby reducing much of the dispersion error generated from the discrepancy between the effective and actual scaled wave numbers. More importantly, application of this upwinding difference scheme can preserve very well the shape of interface for the advection equation, thus avoiding either mass accumulation or depletion. Another main objective of our study is to modify the level set function before performing the re-initialization step so as to improve the level of mass conservation in arbitrarily shaped interfaces which may be merged or split. Furthermore, the

differential-based interpolation immersed boundary formulation is applied to track the solid–fluid interface for the purpose of increasing computational efficiency [37].

This paper is organized as follows: Section 2 presents the smoothing method for the hydrodynamic system which consists of the Navier–Stokes equations and the level set equation. In Section 3, the numerical schemes for solving the Navier–Stokes equations and the level set equation are described. Section 4 describes the immersed boundary method for modeling complex geometry flow in Cartesian grids. Section 5 describes the algorithm of the proposed coupled level set/immersed boundary method. Section 6 presents the predicted results concerning the impact of dam break flow on the solid object. Finally, we will draw some conclusions in Section 7.

2. Mathematical model

2.1. Equation for the free surface modeling

2.1.1. Advection step

In this study an improved interface preserving level set method is developed to predict the time-varying interface (or free surface) in a domain of incompressible fluid flow. At a surface where the value of the level set function is zero, or $\phi(\underline{x}, t) = 0$, both kinematic and dynamic boundary conditions are specified. The kinematic boundary condition is interpreted in Lagrangian sense: for fluid particles sitting on a surface, they will always stay. We can therefore write a mathematically equivalent pure advection equation for the level set function ϕ at an interface that separates the gas and liquid, which is

$$\phi_t + \underline{u} \cdot \nabla \phi = 0, \tag{1}$$

where $\underline{u}$ denotes the flow velocity. Note that the level set function ϕ is initially prescribed to have the following signed distance values in gas and liquid domains

$$\phi = \begin{cases} -d & \text{for } x \in \Omega_{gas} \\ 0 & \text{for } x \in \Gamma_{sf} \\ d & \text{for } x \in \Omega_{liquid}. \end{cases} \tag{2}$$

In Eq. (2), Ω_{gas} and Ω_{liquid} are the gas region and the liquid region, respectively. Γ_{sf} denotes the location of interface and d is the absolute normal distance to the interface.

2.1.2. Intermediate step

Interface motion is represented by the propagation of the zero level set which is embedded in Eq. (1). Although the interface is still represented by the reference value, the other values of ϕ might not be the distances from the interface after calculating Eq. (1), thereby implying that mass is not conserved all the time

$$\int_{\Omega} \mathbf{H}(\phi, t = 0) \, d\Omega - \int_{\Omega} \mathbf{H}(\phi, t) \, d\Omega = \mathcal{H}_{error} \neq 0. \tag{3}$$

In Eq. (3), Ω is a fixed domain. $\mathbf{H}(\phi, t)$ is the smoothed Heaviside function at any time and can be described below

$$\mathbf{H}(\phi, t) = \begin{cases} 0 & ; \text{ if } \phi < -\epsilon \\ \dfrac{1}{(1 + e^{-\frac{3\phi}{\epsilon}})} & ; \text{ if } |\phi| \leq \epsilon \\ 1 & ; \text{ if } \phi > \epsilon. \end{cases} \tag{4}$$

Note that the value of ϵ shown above is chosen to be $2\Delta x$ to conserve the area of a flow bounded by the interface, where Δx denotes the grid spacing. To retain the mass conservation property, the Heaviside function defined in Eq. (4) is modified as

$$\mathbf{H}_{new}(\phi, t)$$
$$= \begin{cases} \mathbf{H}(\phi, t) + \dfrac{\mathcal{H}_{error}}{\mathbf{N_{in}}} & ; \text{ if } 0 < \mathbf{H}(\phi, t) < 1, \\ \mathbf{H}(\phi, t) & ; \text{ if } \mathbf{H}(\phi, t) = 0 \text{ or } \mathbf{H}(\phi, t) = 1, \end{cases} \tag{5}$$

where $\mathbf{N_{in}}$ denotes the total nodal points in the smooth layer (or in the thickness of interface). As a result, application of this intermediate solution step guarantees mass conservation inside the thickness of interface in the sense that $\int_{\Omega} \mathbf{H}(\phi, t = 0) \, d\Omega = \int_{\Omega} \mathbf{H}(\phi_{new}, t) \, d\Omega$. The proof to guarantee mass conservation for this intermediate step has been given in the "Appendix". Note that the values of ϕ from $\mathbf{H}_{new}(\phi, t)$ can be derived by Eq. (4) according to the following equation

$$\phi_{new} = \begin{cases} -\dfrac{1}{3}\ln\left(-\dfrac{\mathbf{H}_{new}(\phi, t) - 1}{\mathbf{H}_{new}(\phi, t)}\right)\epsilon; & \text{if } 0 < \mathbf{H}(\phi, t) < 1, \\ \phi; & \text{if } \mathbf{H}(\phi, t) = 0 \\ & \text{or } \mathbf{H}(\phi, t) = 1. \end{cases} \tag{6}$$

2.1.3. Re-initialization step

To ensure that ϕ remains as a distance function (i.e., satisfying $|\nabla\phi| = 1$) and to conserve mass bounded by the interface, the computed solution ϕ_{new} from Eq. (6) is employed as the initial solution when solving the following re-initialization equation:

$$\phi_\tau + \text{sgn}(\phi_{new})(|\nabla\phi| - 1) = \lambda\delta(\phi)|\nabla\phi|, \tag{7}$$

where the parameter λ shown above is prescribed as that shown in [10]

$$\lambda = -\frac{\int_{\Omega_{i,j}} \delta(\phi)(-\text{sgn}(\phi_{new})(|\nabla\phi| - 1)) \, d\Omega}{\int_{\Omega_{i,j}} \delta^2(\phi)|\nabla\phi| \, d\Omega}. \tag{8}$$

In Eq. (8), $\text{sgn}(\phi_{new}) = 2(\mathbf{H}_{new}(\phi) - \frac{1}{2})$. The Dirac delta function $\delta(\phi)$ shown in Eq. (7) is defined as

$$\delta(\phi) = \begin{cases} 0 & ; \text{if } |\phi| > \epsilon \\ \dfrac{3e^{-\frac{3\phi}{\epsilon}}}{(1 + e^{-\frac{3\phi}{\epsilon}})^2 \, \epsilon} & ; \text{if } |\phi| \le \epsilon. \end{cases} \tag{9}$$

2.2. Navier–Stokes equations

Both liquid and gas fluids are assumed to be incompressible and immiscible. The resulting equations of motion for both fluids separated by an interface are represented by the following dimensionless equations

$$\underline{u}_t + (\underline{u} \cdot \nabla)\underline{u} = \frac{1}{\rho(\phi)}\left[-\nabla p + \frac{1}{Re}\nabla \cdot (2\mu(\phi)\underline{\underline{D}})\right] + \frac{1}{Fr^2}\bar{e}_g, \tag{10}$$

$$\nabla \cdot \underline{u} = 0. \tag{11}$$

Eq. (10) has two dimensionless parameters, which are known as the Reynolds number $Re \,(= \frac{\rho_r u_r l_r}{\mu_r})$ and the Froude number $Fr \,(= \frac{u_r}{\sqrt{gl_r}})$, where u_r, l_r, ρ_r, μ_r are the referenced characteristic values for the respective velocity, length, density and viscosity. The tensor term $\underline{\underline{D}} \,(= \frac{1}{2}(\nabla\underline{u} + \nabla\underline{u}^\mathbf{T}))$ denotes the rate of deformation.

2.3. Physical properties across interface

The fluid properties including density and viscosity across the interface need to be smoothed in order to prevent numerical instabilities near the interface [10]. In this study, the smoothed Heaviside function shown in Eq. (4) is employed to smooth out the density and viscosity jumps in a small zone defined by $|\phi| \le \epsilon$

$$\rho(\phi) = \mathbf{H}(\phi) + \left(\frac{\rho_G}{\rho_L}\right)(1 - \mathbf{H}(\phi)), \tag{12}$$

$$\mu(\phi) = \mathbf{H}(\phi) + \left(\frac{\mu_G}{\mu_L}\right)(1 - \mathbf{H}(\phi)). \tag{13}$$

The subscripts G and L shown above denote the gas and liquid phases, respectively. Note that the continuum surface force (CSF) model should be considered when flow problems under investigation involve surface tension force [21,38,39].

3. Numerical methods

3.1. Numerical method for solving the level set equation

To solve Eq. (1) accurately over a long time, one can employ a high spectral resolution scheme such as the compact difference (CD) scheme or the combined compact difference (CCD) [40] scheme. However, CD and CCD schemes inevitably produce numerical oscillations near discontinuities and possibly lead to breakdown of the flow simulation. In [41], the CCD scheme is used together with the fifth-order compact-reconstruction weighted essentially non-oscillatory (CRWENO5) scheme [42] to avoid numerical oscillation generated around discontinuities. A CCD scheme in the inner grids is coupled with the non-compact explicit scheme applied at the boundary points to solve the wave equations [43]. Different from the CCD scheme presented in [43], our aim in this study is to discrete the level set equation for ϕ using a four-point combined compact difference scheme in the inner grids and the three-point boundary combined compact difference scheme at the boundary points.

3.1.1. Upwinding combined compact difference (UCCD) scheme for spatial derivatives

In the following the combined compact difference scheme for approximating the spatial derivative term ϕ_x is presented. The derivative term ϕ_{xx} is also considered as the unknown variable at each grid point for getting a spectral-like resolution. In a four-point grid stencil with the uniform grid spacing $\Delta x = h$, the employed numerical schemes for $\frac{\partial\phi}{\partial x}$ and $\frac{\partial^2\phi}{\partial x^2}$ are given below

$$a_1 \frac{\partial\phi}{\partial x}\Big|_{i-1} + \frac{\partial\phi}{\partial x}\Big|_i + a_3 \frac{\partial\phi}{\partial x}\Big|_{i+1}$$
$$= \frac{1}{h}(c_1\phi_{i-2} + c_2\phi_{i-1} + c_3\phi_i)$$
$$- h\left(b_1 \frac{\partial^2\phi}{\partial x^2}\Big|_{i-1} + b_2 \frac{\partial^2\phi}{\partial x^2}\Big|_i + b_3 \frac{\partial^2\phi}{\partial x^2}\Big|_{i+1}\right), \tag{14}$$

$$-\frac{1}{8} \frac{\partial^2\phi}{\partial x^2}\Big|_{i-1} + \frac{\partial^2\phi}{\partial x^2}\Big|_i - \frac{1}{8} \frac{\partial^2\phi}{\partial x^2}\Big|_{i+1}$$
$$= \frac{3}{h^2}(\phi_{i-1} - 2\phi_i + \phi_{i+1}) - \frac{9}{8h}\left(-\frac{\partial\phi}{\partial x}\Big|_{i-1} + \frac{\partial\phi}{\partial x}\Big|_{i+1}\right). \tag{15}$$

The coefficients shown in Eq. (15) are derived through the method of Taylor series expansion. Elimination of seven leading truncation error terms by the modified equation analysis enables us to get the formal accuracy order of six [40].

Derivation of the weighting coefficients in Eq. (14) is started from performing Taylor series expansion on the terms ϕ_{i-2}, ϕ_{i-1}, $\frac{\partial\phi}{\partial x}\big|_{i-1}$, $\frac{\partial\phi}{\partial x}\big|_i$, $\frac{\partial\phi}{\partial x}\big|_{i+1}$, $\frac{\partial^2\phi}{\partial x^2}\big|_{i-1}$, $\frac{\partial^2\phi}{\partial x^2}\big|_i$ and $\frac{\partial^2\phi}{\partial x^2}\big|_{i+1}$ with respect to ϕ_i to get the corresponding modified equation. The seven leading truncation error terms derived from the modified equation analysis are then eliminated to get a set of seven algebraic equations. We are still short of one algebraic equation to uniquely get all the introduced coefficients shown in Eq. (14). One way of deriving the eighth equation so as to get a better approximation of the term $\frac{\partial\phi}{\partial x}$ is to reduce numerical error of the accumulative type. We can then retain the theoretical dispersive property of $\frac{\partial\phi}{\partial x}$ [44,45].

Our strategy of achieving the goal of reducing numerical dispersion error is to match the exact and numerical wavenumbers. Use of this underlying approach amounts to equating the effective wavenumbers α' and α'' to those shown on the right-hand sides of Eqs. (16) and (17) [44]. The equations for $\alpha'h$ and $\alpha''h$ are as follows

$$\mathbf{i}\alpha'h\,(a_1e^{-\mathbf{i}\alpha h} + 1 + a_3e^{\mathbf{i}\alpha h}) = (c_1e^{-2\mathbf{i}\alpha h} + c_2e^{-\mathbf{i}\alpha h} + c_3)$$
$$- (\mathbf{i}\alpha''h)^2(b_1e^{-\mathbf{i}\alpha h} + b_2 + b_3e^{\mathbf{i}\alpha h}), \tag{16}$$
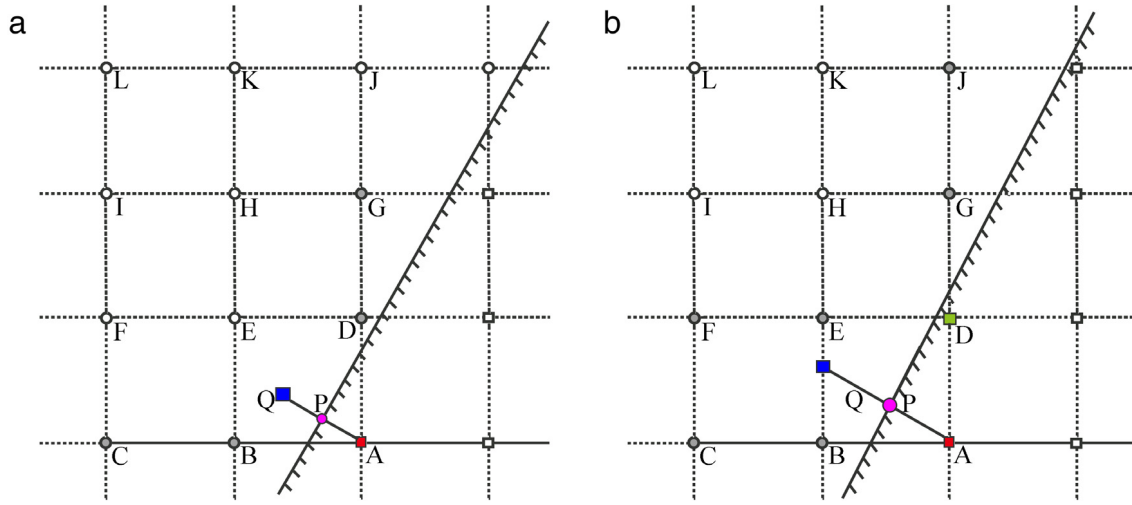
Fig. 1. Schematic of the differential interpolation scheme. (a) For the cell involving three fluid nodes (i.e. B,E,D nodes); (b) For the cell involving two fluid nodes (i.e. B,E nodes). Note that the values used for the interpolation are marked by the gray circles.

$$(\mathbf{i}\alpha'' h)^2 \left(-\frac{1}{8} e^{-\mathbf{i}\alpha h} + 1 - \frac{1}{8} e^{\mathbf{i}\alpha h} \right) = (3e^{-\mathbf{i}\alpha h} - 6 + 3e^{\mathbf{i}\alpha h})$$
$$- \mathbf{i}\alpha' h \left(-\frac{9}{8} e^{-\mathbf{i}\alpha h} + \frac{9}{8} e^{\mathbf{i}\alpha h} \right). \tag{17}$$

The expression of $\alpha' h$ can be directly derived from Eqs. (16) and (17). It is worthy to note here that the real and imaginary parts of the numerical modified (or scaled) wavenumber $\alpha' h$ account for the numerically generated dispersion error (or phase error) and the dissipation error (or amplitude error), respectively.

To improve the dispersive accuracy of α', the exact value of αh should be very close to $\Re[\alpha' h]$, where $\Re[\alpha' h]$ denotes the real part of $\alpha' h$. To achieve this goal, the positive value error function $E(\alpha)$ defined below should be very small over the integration interval for the modified wavenumber αh

$$E(\alpha) = \int_0^{\frac{7\pi}{8}} \left[W \cdot (\alpha h - \Re[\alpha' h]) \right]^2 d(\alpha h). \tag{18}$$

Note that several integration ranges have been numerically studied so as to find the best one that can render the smallest value of E. The weighting function W in Eq. (18) is chosen to be the denominator of $(\alpha h - \Re[\alpha' h])$ [46]. This choice facilitates us to integrate $E(\alpha)$ exactly. To make the error function $E(\alpha)$ defined in $0 \leq \alpha h \leq \frac{7\pi}{8}$ to be positive and minimal, the extreme condition given by $\frac{\partial E}{\partial c_3} = 0$ shall be enforced. The constraint equation enforced in this way for maximizing the dispersion accuracy is used together with the other seven algebraic equations derived from the modified equation analysis to get not only a smaller dissipation error but also an improved dispersion accuracy.

The resulting eight introduced unknown coefficients can be uniquely determined as $a_1 = 0.88825179$, $a_3 = 0.04922965$, $b_1 = 0.15007240$, $b_2 = -0.25071279$, $b_3 = -0.01241647$, $c_1 = 0.01666172$, $c_2 = -1.97080488$ and $c_3 = 1.95414316$ from the underlying strategy of reducing both dispersion and dissipation errors. The upwinding scheme developed theoretically in the four stencil points $i-2, i-1, i$ and $i+1$ for $\frac{\partial \phi}{\partial x}$ has the spatial accuracy of order six according to the derived modified equation given below

$$\frac{\partial \phi}{\partial x} = \frac{\partial \phi}{\partial x}\Big|_{exact} + 0.424003657 \times 10^{-6} h^6 \frac{\partial^7 \phi}{\partial x^7} + H.O.T. \tag{19}$$
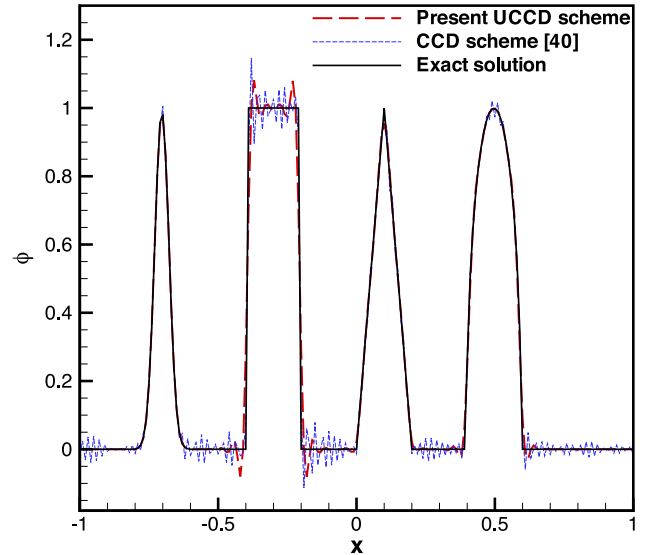

Fig. 2. The predicted results for linear advection problem are plotted at $t = 2$.
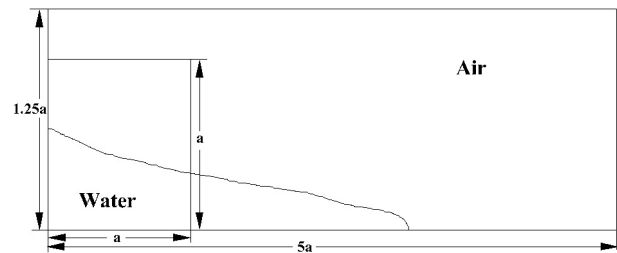

Fig. 3. Schematic of the initial condition for the investigated 2D dam break flow.

For $\underline{u} < 0$, the proposed four-point UCCD scheme can be similarly derived.

For the present UCCD scheme, the first derivative term $\frac{\partial \phi}{\partial x}|_1$ at the left boundary point x_1 is approximated by the following formula

$$\frac{\partial \phi}{\partial x}\Big|_1 + \overline{\alpha}_1 \frac{\partial \phi}{\partial x}\Big|_2 + \overline{\beta}_1 h \frac{\partial^2 \phi}{\partial x^2}\Big|_2 = \frac{1}{h}(\overline{a}_1 \phi_1 + \overline{b}_1 \phi_2 + \overline{c}_1 \phi_3). \tag{20}$$
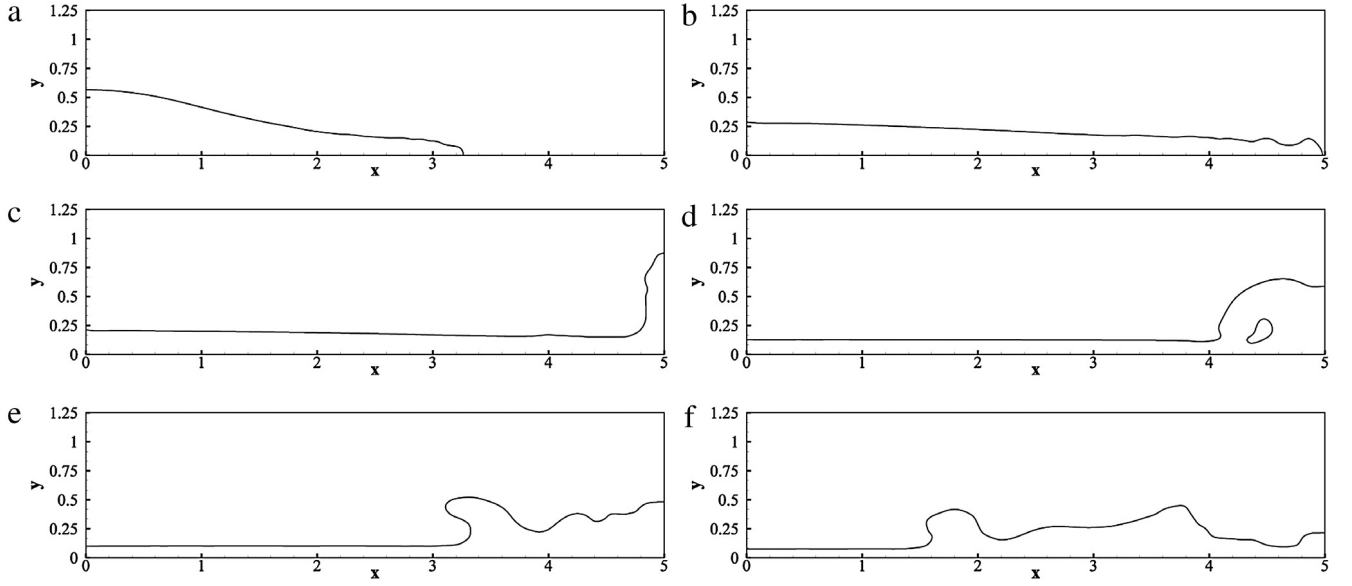
Fig. 4. The predicted solutions at $Re = 42\,796$ in 300×75 grids. (a) $t = 2$; (b) $t = 3.75$; (c) $t = 4.7$; (d) $t = 7.3$; (e) $t = 8.8$; (f) $t = 11.5$.
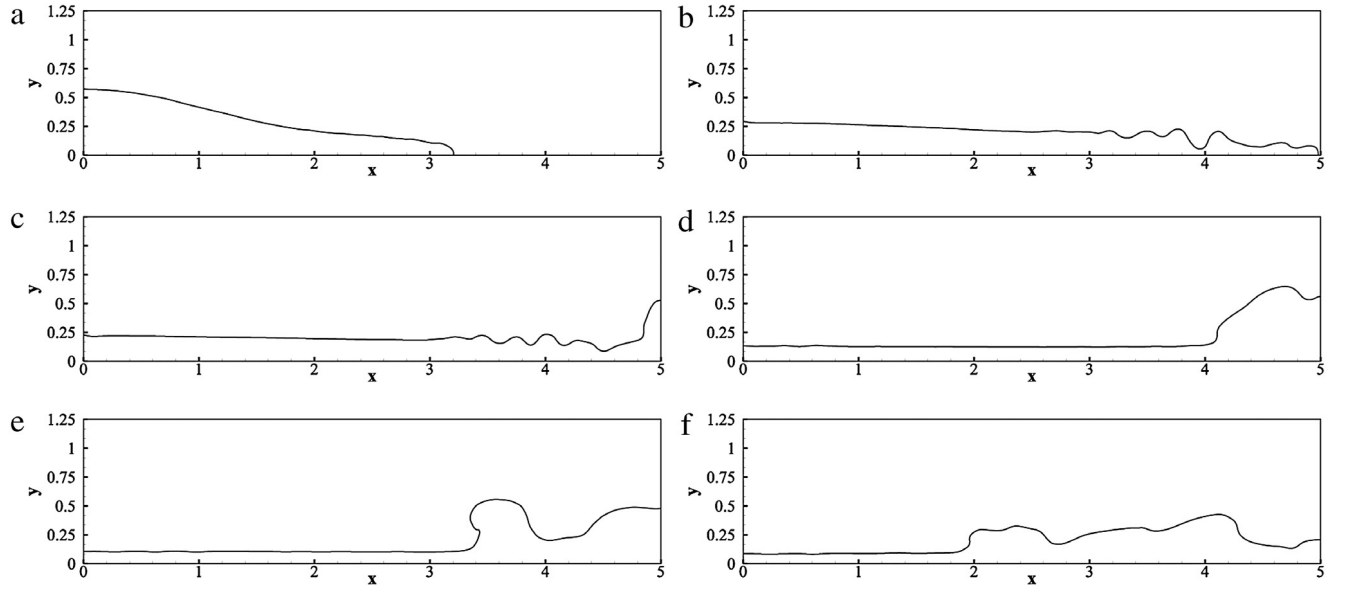

Fig. 5. The predicted solutions at $Re = 122\,000$ in 300×75 grids. (a) $t = 2$; (b) $t = 3.75$; (c) $t = 4.7$; (d) $t = 7.3$; (e) $t = 8.8$; (f) $t = 11.5$.

The Taylor series expansions is used in Eq. (20) for the terms $\frac{\partial \phi}{\partial x}|_2$, $\frac{\partial \phi^2}{\partial x^2}|_2$, ϕ_1, ϕ_2 and ϕ_3. Therefore, the leading five truncation error terms are eliminated in the modified equation to get the following set of algebraic equations:

$$\bar{a}_1 + \bar{b}_1 + \bar{c}_1 = 0, \tag{21}$$

$$\bar{b}_1 + 2\bar{c}_1 - \bar{\alpha}_1 = 1, \tag{22}$$

$$\frac{1}{2}\bar{b}_1 + 2\bar{c}_1 - \bar{\alpha}_1 - \bar{\beta}_1 = 0, \tag{23}$$

$$\frac{1}{6}\bar{b}_1 + \frac{4}{3}\bar{c}_1 - \frac{1}{2}\bar{\alpha}_1 - \bar{\beta}_1 = 0, \tag{24}$$

$$\frac{1}{24}\bar{b}_1 + \frac{2}{3}\bar{c}_1 - \frac{1}{6}\bar{\alpha}_1 - \frac{1}{2}\bar{\beta}_1 = 0. \tag{25}$$

The resulting five unknown coefficients shown in Eq. (20) can be determined as $\bar{\alpha}_1 = 2, \bar{\beta}_1 = -1, \bar{a}_1 = -\frac{7}{2}, \bar{b}_1 = 4, \bar{c}_1 = -\frac{1}{2}$. We also approximated the first derivative term at the right boundary point x_N

$$\frac{\partial \phi}{\partial x}|_N + \bar{\alpha}_1 \frac{\partial \phi}{\partial x}|_{N-1} - \bar{\beta}_1 h \frac{\partial^2 \phi}{\partial x^2}|_{N-1}$$

$$= -\frac{1}{h}(\bar{a}_1 \phi_N + \bar{b}_1 \phi_{N-1} + \bar{c}_1 \phi_{N-2}), \tag{26}$$

where N denotes the number of grid points along x-direction. The coefficients shown in Eq. (26) can be also determined through the Taylor series expansion with respect to ϕ_N. It is note that both Eqs. (20) and (26) have the truncation error term $-\frac{22}{5!}h^4 \frac{\partial^5 \phi}{\partial x^5}$. The second derivative terms approximated at the two boundary points x_1 and x_N are summarized below:
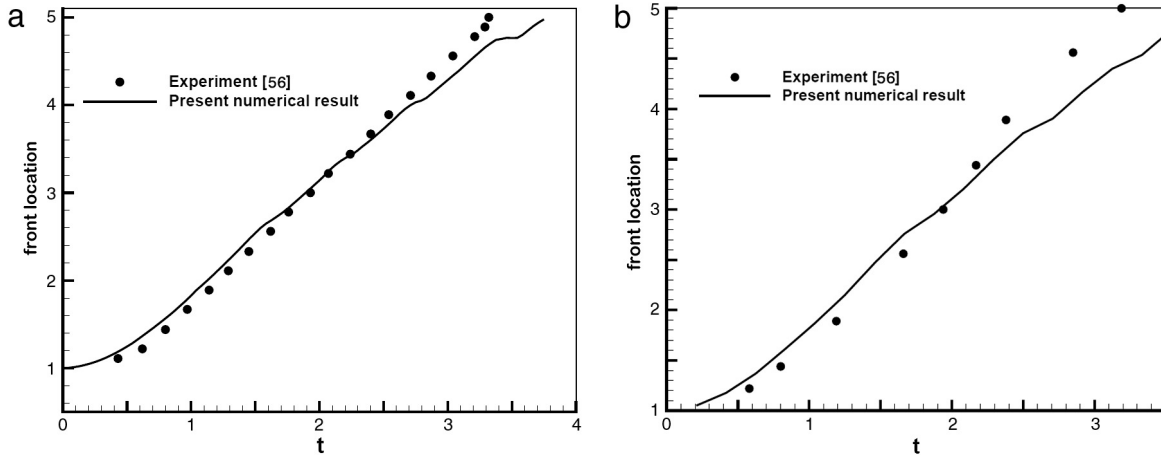
Fig. 6. The plots of the front location of the dam break flow against time at different Reynolds numbers. (a) $Re = 42\,796$; (b) $Re = 122\,000$.
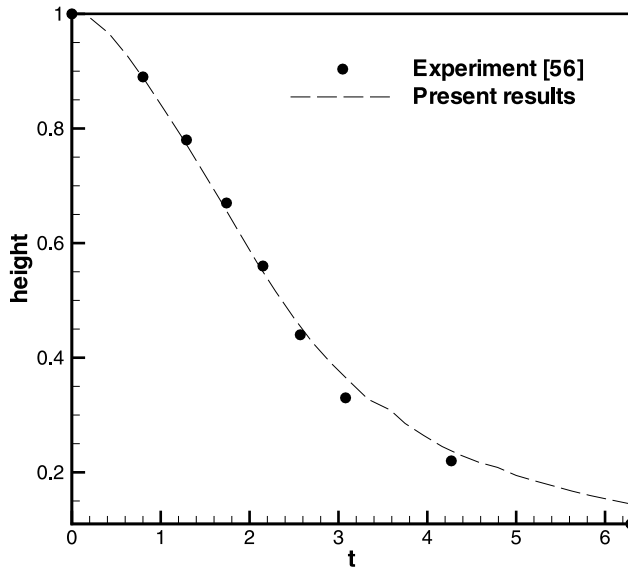

Fig. 7. Comparison of the water columns for the dam break flow investigated at $Re = 42\,796$.

$$h\left(\frac{\partial^2 \phi}{\partial x^2}\right)_1 + \overline{\alpha}_2 h\left(\frac{\partial^2 \phi}{\partial x^2}\right)_2 + \overline{\beta}_2 \left(\frac{\partial \phi}{\partial x}\right)_2$$
$$= \frac{1}{h}(\overline{a}_2\phi_1 + \overline{b}_2\phi_2 + \overline{c}_2\phi_3), \tag{27}$$

$$h\left(\frac{\partial^2 \phi}{\partial x^2}\right)_N + \overline{\alpha}_2 h\left(\frac{\partial^2 \phi}{\partial x^2}\right)_{N-1} - \overline{\beta}_2 \left(\frac{d\phi}{dx}\right)_{N-1}$$
$$= \frac{1}{h}(\overline{a}_2\phi_N + \overline{b}_2\phi_{N-1} + \overline{c}_2\phi_{N-2}), \tag{28}$$

where $\overline{\alpha}_2 = 5, \overline{\beta}_2 = -6, \overline{a}_2 = 9, \overline{b}_2 = -12$ and $\overline{c}_2 = 3$. The truncation error term is $-\frac{14}{5!}h^4\frac{\partial^5 \phi}{\partial x^5}$ for Eqs. (27) and (28). The above proposed UCCD scheme, which uses Eqs. (20) and (27) for $i = 1$, Eqs. (26) and (28) for $i = N$, and Eqs. (14), (15) for $i = 2, 3, 4, \cdots N - 1$, forms a $2N \times 2N$ matrix system. These matrix equations can be effectively solved by the twin-forward elimination and twin-backward substitution solution solvers [40].

3.1.2. Symplectic Runge–Kutta scheme for temporal derivatives

The temporally sixth-order accurate implicit symplectic Runge–Kutta scheme [47] is employed to solve the following ordinary differential equation with a function $F(\equiv -\underline{u} \cdot \nabla\phi)$

$$\frac{d\phi}{dt} = F(\phi). \tag{29}$$

Given the solution ϕ^n at $t = n\Delta t$, the solution ϕ^{n+1} is obtained iteratively from the procedures given below. Calculation of the solutions from Eq. (29) is started from the guessed values $\phi^{(i)}$ for ϕ^n, where i=1 to 3, to calculate $F^{(i)}$. These computed values of $F^{(i)}$ ($i = 1, 2, 3$) are then substituted into the implicit equations given below to update the values of $\phi^{(i)}$ (i= 1 to 3)

$$\phi^{(1)} = \phi^n + \Delta t \left[\frac{5}{36}F^{(1)} + \left(\frac{2}{9} + \frac{2\widetilde{c}}{3}\right)F^{(2)} \right.$$
$$\left. + \left(\frac{5}{36} + \frac{\widetilde{c}}{3}\right)F^{(3)}\right], \tag{30}$$

$$\phi^{(2)} = \phi^n + \Delta t \left[\left(\frac{5}{36} - \frac{5\widetilde{c}}{12}\right)F^{(1)} + \frac{2}{9}F^{(2)} \right.$$
$$\left. + \left(\frac{5}{36} + \frac{5\widetilde{c}}{12}\right)F^{(3)}\right], \tag{31}$$

$$\phi^{(3)} = \phi^n + \Delta t \left[\left(\frac{5}{36} - \frac{\widetilde{c}}{3}\right)F^{(1)} \right.$$
$$\left. + \left(\frac{2}{9} - \frac{2\widetilde{c}}{3}\right)F^{(2)} + \frac{5}{36}F^{(3)}\right]. \tag{32}$$

where $\widetilde{c} = \frac{1}{2}\sqrt{\frac{3}{5}}$. Note that $F^{(i)}(i = 1, 2, 3)$ shown above represent the values of F at $t = n + (\frac{1}{2} + \widetilde{c})\Delta t$, $t = n + \frac{1}{2}\Delta t$, and $t = n + (\frac{1}{2} - \widetilde{c})\Delta t$, respectively. As the difference of the solutions computed from any two consecutive iterations becomes a negligibly small magnitude, calculation of the values of $F^{(i)}$ from Eqs. (30)–(32) is terminated. Upon reaching the specified tolerance, which is 10^{-6}, the solution at the time $t = (n + 1)\Delta t$ is obtained as $\phi^{n+1} = \phi^n + \frac{\Delta t}{9}\left[\frac{5}{2}F^{(1)} + 4F^{(2)} + \frac{5}{2}F^{(3)}\right]$.

3.2. Numerical implementation of the re-initialization equation

The fifth-order weighted essentially non-oscillatory (WENO5) scheme [48] is applied to approximate the spatial derivative term shown in the re-initialization equation (7). As for the temporal
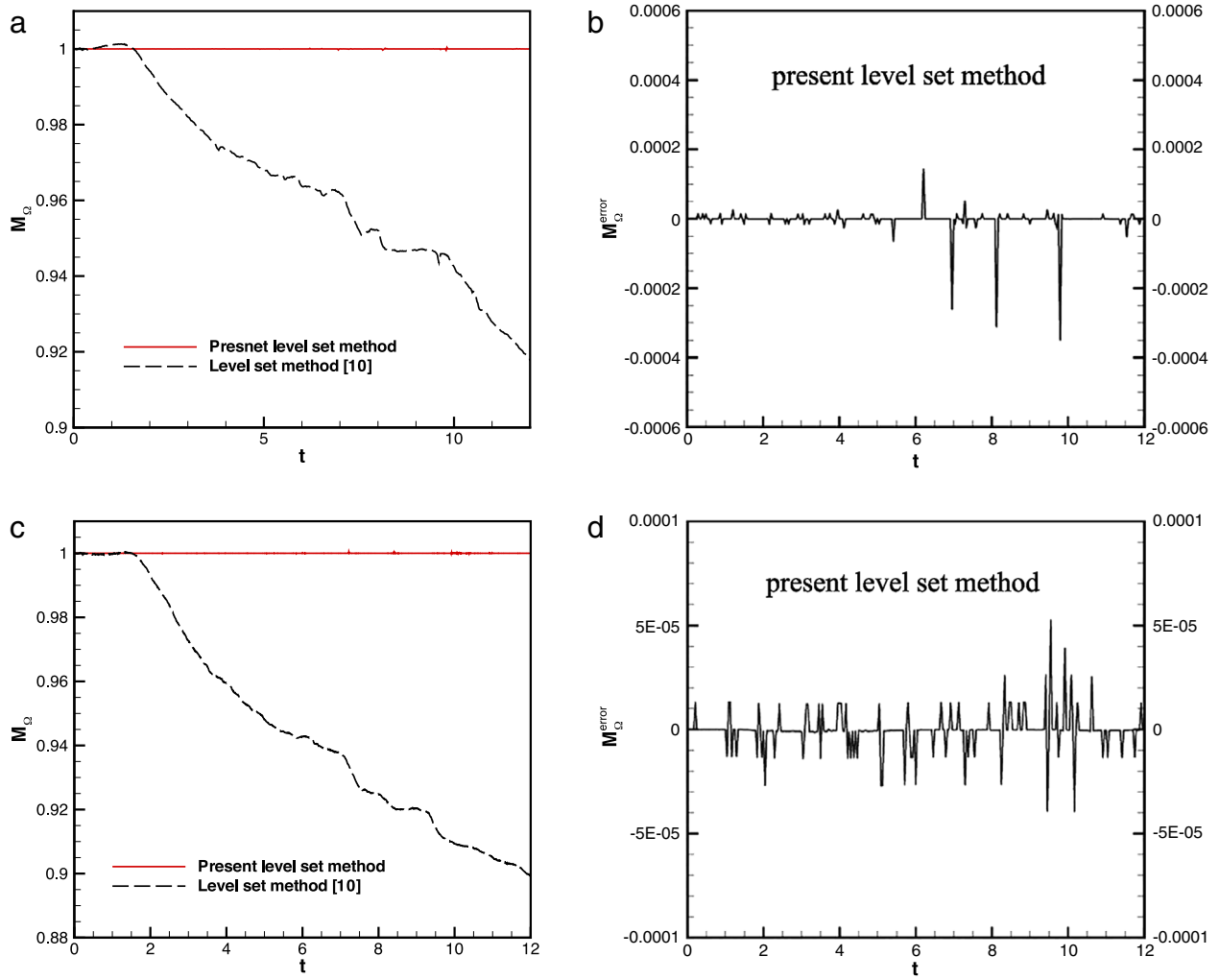
Fig. 8. The values of $\mathbf{M}_\Omega$ and $\mathbf{M}_\Omega^{error}$ are plotted with respect to the dimensionless time t for the dam break flow on a dry bed. (a) and (b) $Re = 42\,795$; (c) and (d) $Re = 122\,000$.
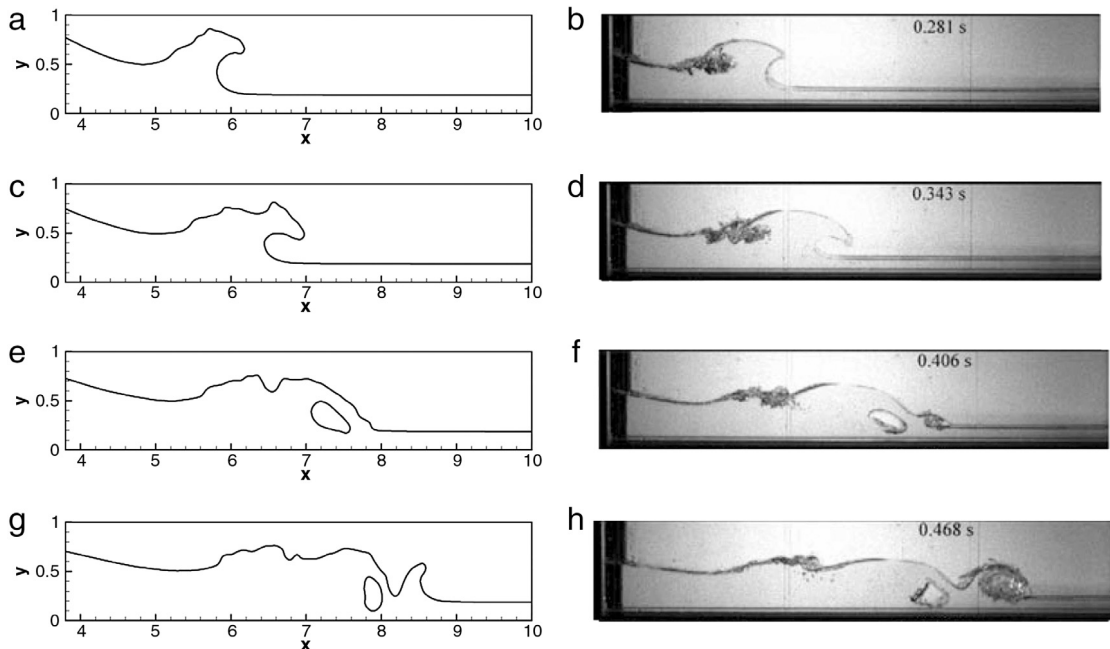

Fig. 9. Comparison of the numerical and experimental results on a wet bed at different dimensionless times. (a), (c), (e), (g) present numerical results; (b), (d), (f), (h) represent experimental results [57].
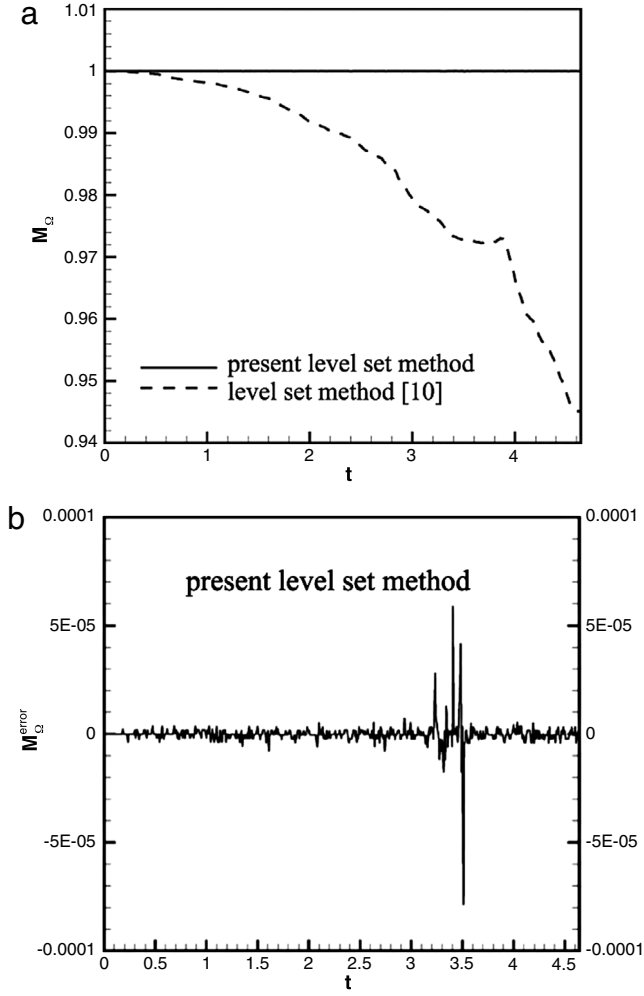
Fig. 10. Justification of the predicted mass conservation property for the dam break problem on a wet bed at $t = 0.343$ s. (a) $\mathbf{M}_\Omega$; (b) $\mathbf{M}_\Omega^{error}$.

derivative term shown in the following equation for ϕ

$$\frac{d\phi}{d\tau} = L(\phi) = -\text{sgn}(\phi_{new})(|\nabla\phi| - 1) + \lambda\delta(\phi)|\nabla\phi|, \quad (33)$$

the third-order TVD Runge–Kutta (TVD-RK3) scheme [49] is applied. The solution of the above ordinary differential equation is solved through the algorithm consisting of the following three steps

$$\phi^{(1)} = \phi^{(n)} + \Delta\tau L(\phi^{(0)}), \quad (34)$$

$$\phi^{(2)} = \frac{3}{4}\phi^{(n)} + \frac{1}{4}\phi^{(1)} + \frac{1}{4}\Delta\tau L(\phi^{(1)}), \quad (35)$$

$$\phi^{(n+1)} = \frac{1}{3}\phi^{(n)} + \frac{2}{3}\phi^{(2)} + \frac{2}{3}\Delta\tau L(\phi^{(2)}). \quad (36)$$

4. Immersed boundary method

How to prescribe the nodal forces along the immersed boundary is the key to determine the success of applying the immersed boundary method. In general, these forcing points are not necessarily located at the boundary of immersed object. It is therefore required to interpolate velocity in all solid–fluid cells. However, the boundary treatment using algebra-based approaches may lead

to numerical instability. To resolve this kind of instability problem motivates the development of the class of methods without the need of performing interpolation that is indispensable in the algebraically-interpolated method [37].

The present IB method can be used efficiently in planar and curved boundaries as shown in Fig. 1(a) and (b). We define the value u_Q at point Q, which is the image point of the ghost point A through the boundary point P. It follows that the length between points A and P (or $\overline{AP}$) is equal to the length between points P and Q (or $\overline{PQ}$). The value u_A is derived in terms of u_Q and u_P as follows by performing Taylor series expansion along the direction orthogonal to the immersed boundary

$$u_A = 2u_P - u_Q. \quad (37)$$

In what follows, we will determine the value u_Q at Q.

The following advection equation will be employed to calculate the value of u along the direction normal to the immersed boundary [37]

$$\frac{\partial u}{\partial \tau} + \underline{n} \cdot \nabla u = 0. \quad (38)$$

In the above, τ is the artificial time and $\underline{n}$ denotes the unit normal vector. By solving Eq. (38), one can transport the known value to the ghost point placed inside the solid. For example, we evaluate u_Q using the differential Eq. (38) at the ghost point A by means of $\Delta\tau = \overline{APQ} = 2\overline{AP}$. Eq. (38) can be discretized by the following first-order upwind scheme

$$\left(\frac{u_A^{\tau+1} - u_A^\tau}{\Delta\tau} + O(\Delta\tau)\right) + \left(n_x \frac{u_A^\tau - u_B^\tau}{\Delta x} + O(\Delta x)\right)$$
$$+ \left(n_y \frac{u_D^\tau - u_A^\tau}{\Delta y} + O(\Delta y)\right) = 0, \quad (39)$$

where Δx and Δy are the grid spacings along the x- and y-direction, respectively. However, the value u_A^τ is unknown since A is a solid ghost point.

To determine the unknown value u_A^τ, the following extrapolation equation given in [50] is used

$$\frac{\partial u}{\partial \tau^*} + n_x(\Delta x u_{xx}') + n_y(\Delta y u_{yy}') = 0. \quad (40)$$

The values of u_{xx}' and u_{yy}' will be calculated below. Define

$$u_{xx}(i, j) = \frac{(u_{i,j} - 2u_{i-1,j} + u_{i+1,j})}{\Delta x^2}$$

$$u_{yy}(i, j) = \frac{(u_{i,j} - 2u_{i,j-1} + u_{i,j+1})}{\Delta y^2}$$

we can then derive

$u_{xx}'(i, j) = u_{xx}(i - 1, j)$ if $n_x(i, j) \geq 0$;
   else $u_{xx}'(i, j) = -u_{xx}(i + 1, j)$
$u_{yy}'(i, j) = u_{yy}(i, j - 1)$ if $n_y(i, j) \geq 0$;
   else $u_{yy}'(i, j) = -u_{yy}(i, j + 1)$.

By solving Eq. (40) until the steady-state solution is reached, the second-order accurate extrapolation along the characteristic direction can be obtained at the ghost points. It is noted that if $n_x = 0$ or $n_y = 0$, the above derivation will be reduced to the one-dimensional second-order extrapolation along x or y direction. Numerical results confirm that the solution of second-order accuracy for $u_A^{\tau+1}$ can be calculated from Eq. (39) provided that u_A^τ is obtained by solving Eq. (40) to get the steady state solution.

The overall solution procedures of the present method are summarized below [37]:

(I) calculate the extrapolated velocity u_A^τ at point A by solving Eq. (40) to get the steady state solution.
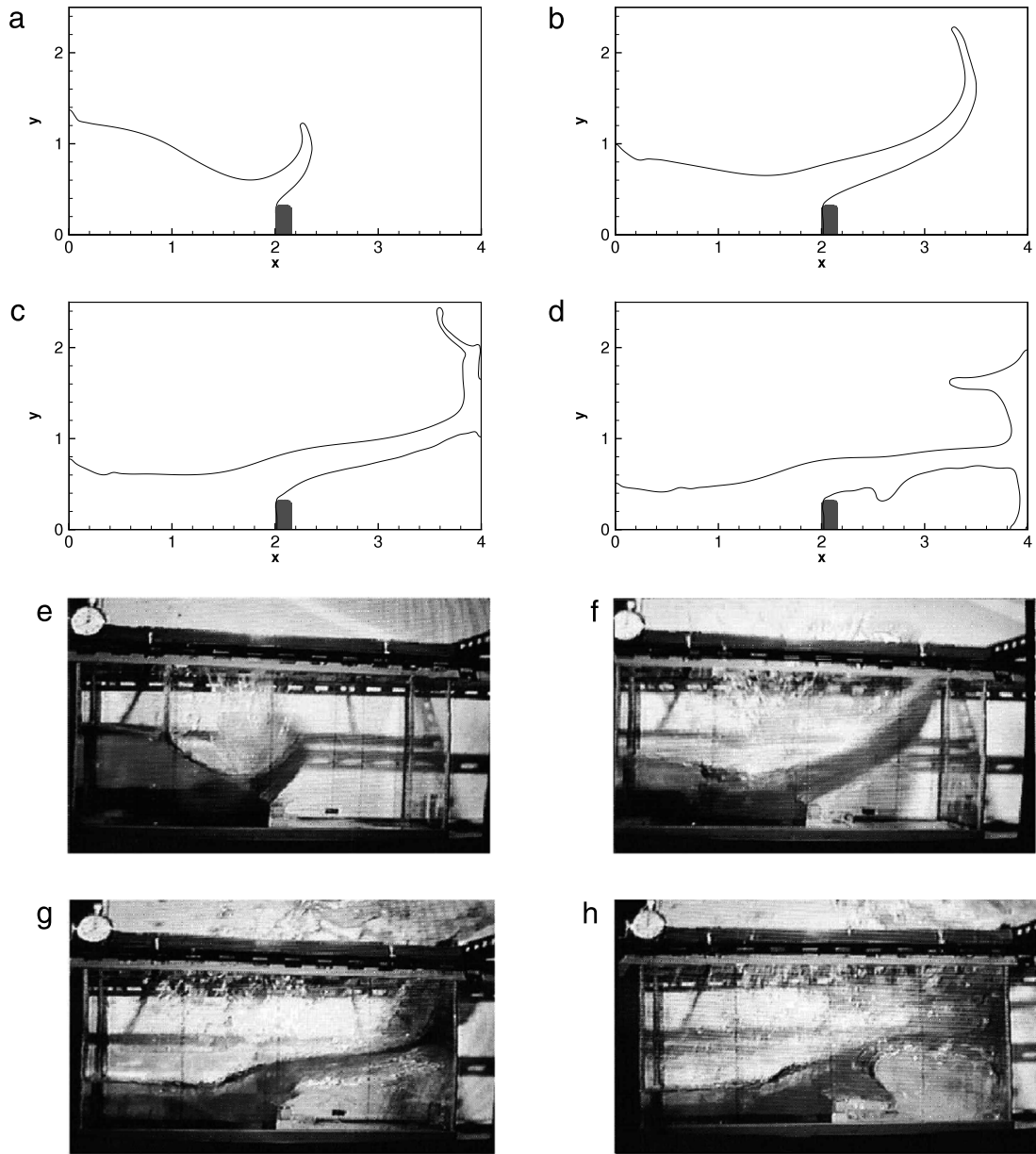
Fig. 11. The predicted free surfaces for the dam break problem at different times. (a) $t = 0.2$ s; (b) $t = 0.3$ s; (c) $t = 0.4$ s; (d) $t = 0.5$ s; (e) $t = 0.2$ s [58]; (f) $t = 0.3$ s [58]; (g) $t = 0.4$ s [58]; (h) $t = 0.5$ s [58].

(II) calculate $u_A^{\tau+1}$ at point A by solving Eq. (38) at the artificial time $\tau = 2\overline{AP}$.

(III) set $u_Q = u_A^{\tau+1}$ and calculate the intermediate velocity u_A at point A by using Eq. (37).

5. Incompressible two-phase flow solver

5.1. Approximation of the convection terms in the momentum equations

Approximation of the convective terms in flow equations needs to take the upwinding nodal solutions along the flow direction into a favorable consideration. A sixth-order upwinding combined compact difference scheme described in Section 3.1.1 for $\phi = u$ (or v) is employed to approximate the first-order derivative terms in the equations. Our primary aim is to enhance convective stability and increase dispersive accuracy at the same time when solving the Navier–Stokes equations.

5.2. Projection method for the two phase flow system

The projection method [51,52] is an effective method in solving the time-dependent incompressible flow solutions. The advantage of the projection method employed in this study is that the computation of velocity and pressure fields can be decoupled. In [53], the second order projection method for variable density incompressible flows is described. Development of this method is based on a second order fractional step scheme in which diffusion–convection terms are advanced without enforcing the incompressibility condition. The resulting intermediate velocity field is then projected onto the space of a discretely divergence free vector field. Based on the idea of the projection method given in [51], the computational procedures are summarized as follows:

(**Step 1**) Set $\phi_0 = 1$ in the liquid while $\phi_0 = -1$ in the gas. Initialize the level set function ϕ by solving the initialization equation given
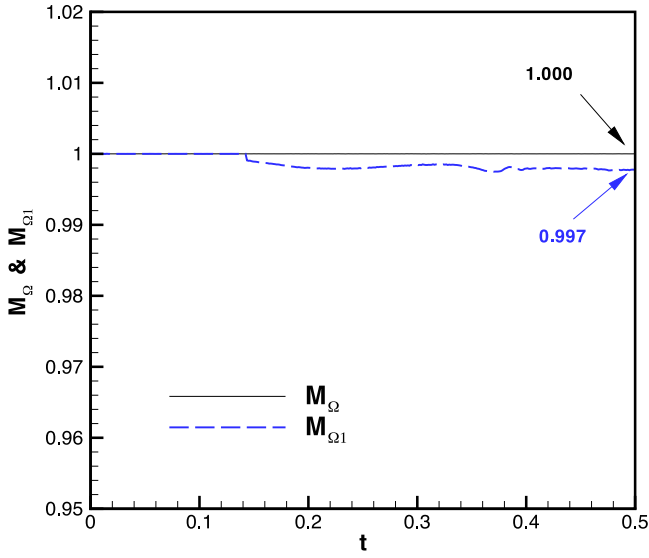
Fig. 12. The ratios defined in Eqs. (46) and (47) are plotted with respect to time t for the calculation carried out in 400×240 grids.

below

$$\phi_\tau + \text{sgn}(\phi_0)(|\nabla\phi| - 1) = 0. \tag{41}$$

Given the solution obtained at a time $T = L_D$, which is the largest length of the computational domain, we set the computed value of ϕ as ϕ_0.

(**Step 2**) Define the fluid properties of density $\rho(\phi)$ and viscosity $\mu(\phi)$ described in Section 2.3.

(**Step 3**) Calculate the intermediate velocity $\underline{u}^*$ by solving the following momentum equation in the fluid-domain

$$\frac{\underline{u}^* - \underline{u}^n}{\Delta t} = -(\underline{u}^n \cdot \nabla)\underline{u}^n + \frac{\nabla \cdot (2\mu(\phi)\underline{\underline{D}}^n)}{\rho(\phi)} + \frac{1}{Fr^2}\bar{e}_g. \tag{42}$$

(**Step 4**) Calculate the extrapolated intermediate velocity $\underline{u}_A^*$ (see Fig. 1) at the solid points that are near the flow domain by the immersed boundary method presented in Section 4.

(**Step 5**) Derive the following Poisson equation for p^{n+1}

$$\nabla \cdot \frac{\nabla p^{n+1}}{\rho(\phi)} = \frac{\nabla \cdot \underline{u}^*}{\Delta t}, \tag{43}$$

by taking the divergence and requiring that $\nabla \cdot \underline{u}^{n+1} = 0$.

(**Step 6**) Approximate Eq. (43) for the 2D situation by

$$\left(\frac{p_{i+1,j}^{n+1} - p_{i,j}^{n+1}}{\rho_{i+\frac{1}{2},j}\Delta x^2}\right) - \left(\frac{p_{i,j}^{n+1} - p_{i-1,j}^{n+1}}{\rho_{i-\frac{1}{2},j}\Delta x^2}\right) + \left(\frac{p_{i,j+1}^{n+1} - p_{i,j}^{n+1}}{\rho_{i,j+\frac{1}{2}}\Delta y^2}\right)$$
$$- \left(\frac{p_{i,j}^{n+1} - p_{i,j-1}^{n+1}}{\rho_{i,j-\frac{1}{2}}\Delta y^2}\right)$$
$$= \frac{1}{\Delta t}\left(\frac{u_{i+1,j}^* - u_{i-1,j}^*}{\Delta x} + \frac{v_{i,j+1}^* - v_{i,j-1}^*}{\Delta y}\right). \tag{44}$$

The above implicit equation can be solved using the Gauss–Seidel iterative solver to obtain $p_{i,j}^{n+1}$. Note that the harmonic mean instead of arithmetic mean is employed to calculate the face values $\rho_{i-\frac{1}{2},j}$, $\rho_{i+\frac{1}{2},j}$, $\rho_{i,j-\frac{1}{2}}$ and $\rho_{i,j+\frac{1}{2}}$.

(**Step 7**) Correct the intermediate velocity to obtain the final solution $\underline{u}^{n+1}$

$$\frac{\underline{u}^{n+1} - \underline{u}^*}{\Delta t} = -\frac{\nabla p^{n+1}}{\rho(\phi)}. \tag{45}$$
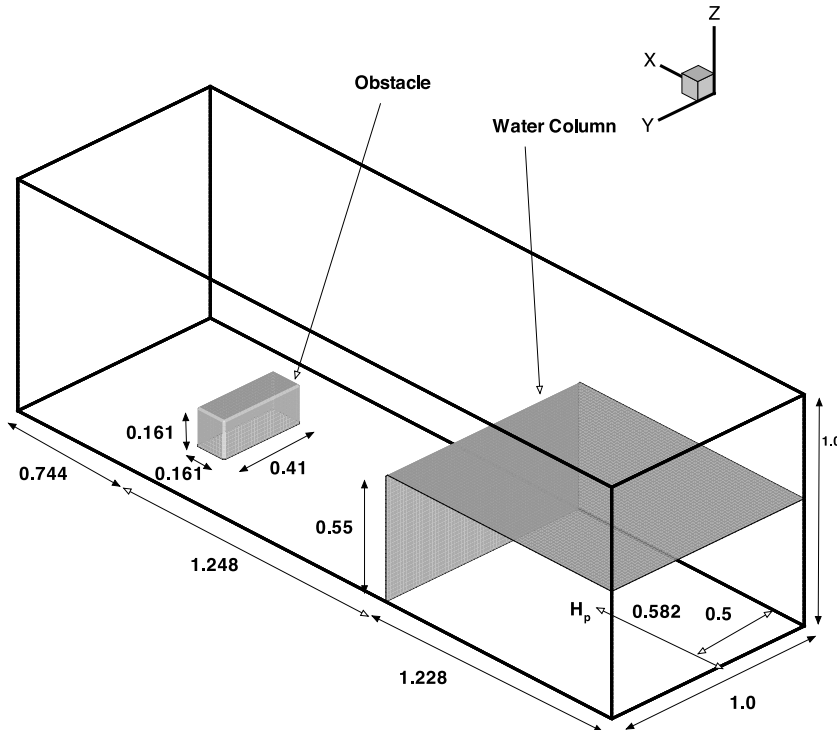

Fig. 13. Schematic of the 3D dam break flow over a rectangle obstacle.
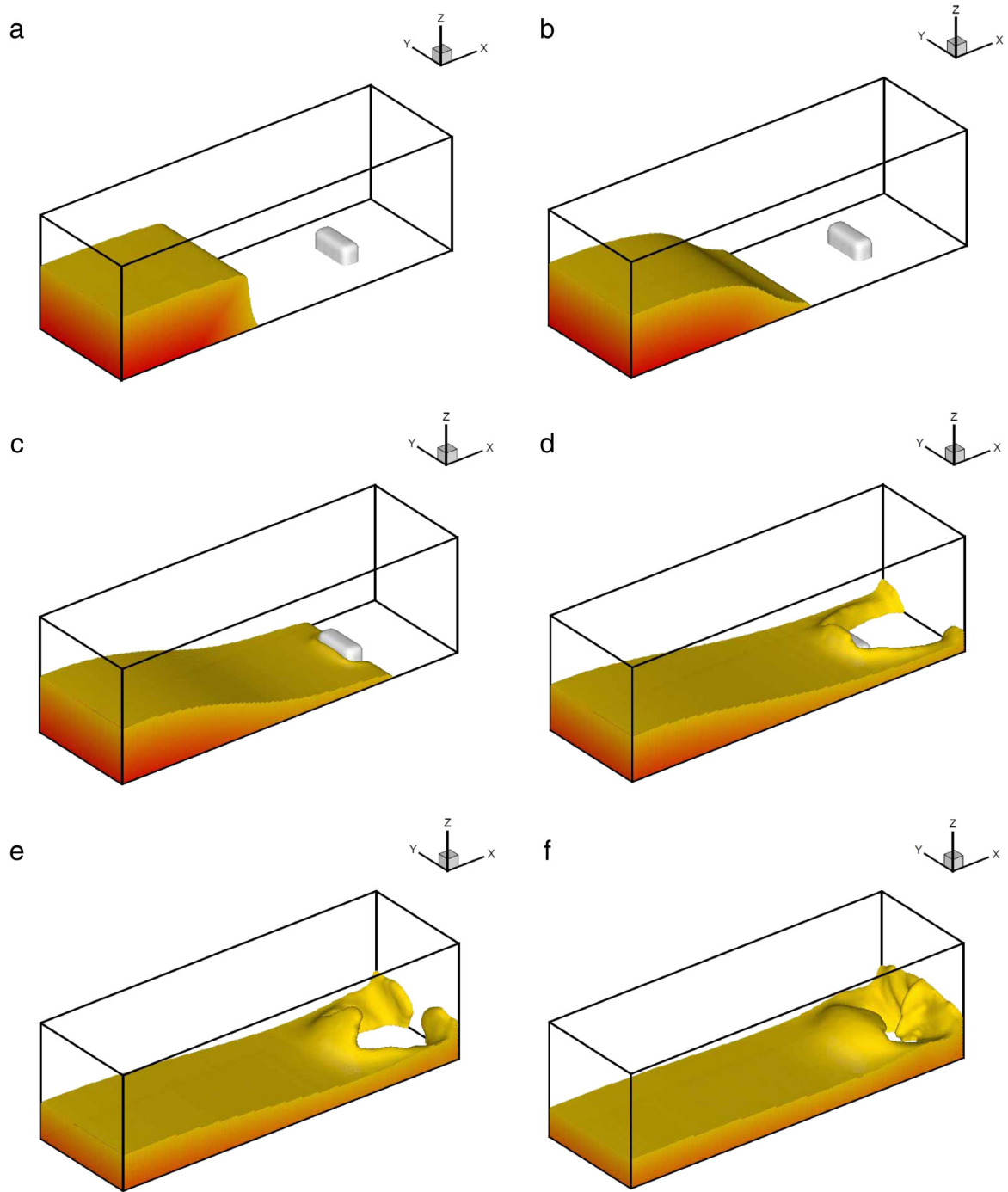
Fig. 14. The predicted time-evolving free surfaces for the 3D dam break flow over a rectangle obstacle. (a) $t = 0.125$ s; (b) $t = 0.25$ s; (c) $t = 0.5$ s; (d) $t = 0.75$ s; (e) $t = 1.0$ s; (f) $t = 1.25$ s.

(**Step 8**) Solve Eq. (1) by the CCD scheme described in Section 3.1.1 with the symplectic Runge–Kutta time marching scheme described in Section 3.1.2 to obtain ϕ^{n+1}.

(**Step 9**) Calculate the new smoothed Heaviside function $\mathbf{H}(\phi_{new})$ by Eq. (5). If $\mathbf{H}_{new}(\phi, t) > 1$, set $\mathbf{H}_{new}(\phi, t) = 1$, if $\mathbf{H}_{new}(\phi, t) < 0$, set $\mathbf{H}_{new}(\phi, t) = 0$.

(**Step 10**) Calculate the new level set value ϕ_{new}^{n+1} by Eq. (6).

(**Step 11**) Re-initialize the level set function ϕ_{new}^{n+1} by solving Eq. (7) described in Section 2.1.3.

(**Step 12**) Repeat the calculations from Step 2 to Step 11 for one time loop.

6. Numerical results

The performance for the CCD and UCCD schemes is shown in Section 6.1 by a advection test. Two dam break problems in Section 6.2 are chosen to show the ability of the proposed method to solve the problems without taking solid object into account. We measure the mass and its errors, respectively, as

$$\mathbf{M}_{\Omega} = \frac{\int_{\Omega} \mathbf{H}(\phi, t) \, d\Omega}{\int_{\Omega} \mathbf{H}(\phi, t = 0) \, d\Omega}, \tag{46}$$
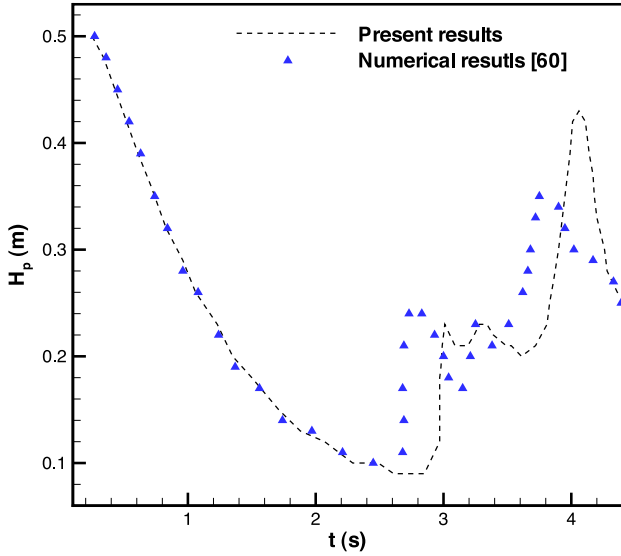
Fig. 15. The predicted water depth at the point H_p is plotted with respect to time.
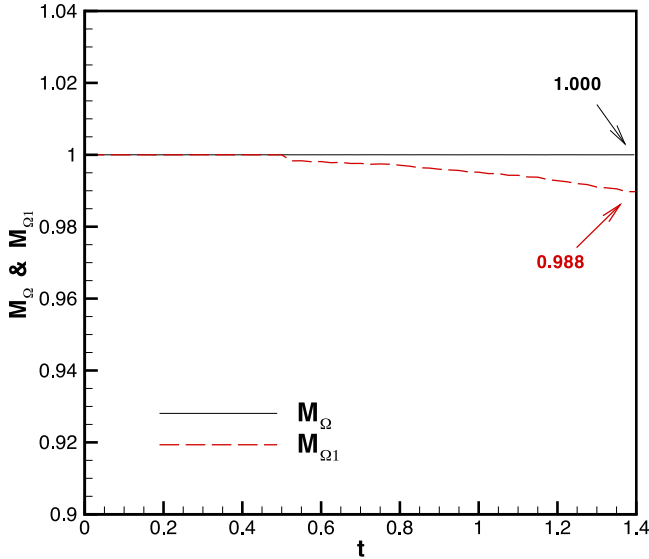

Fig. 16. The ratios defined in Eqs. (46) and (47) are plotted with respect to time t for the calculation carried out in $256 \times 80 \times 80$ grids.

and

$$\mathbf{M}_\Omega^{error} = \frac{\int_\Omega \mathbf{H}(\phi, t)\, d\Omega - \int_\Omega \mathbf{H}(\phi, t = 0)\, d\Omega}{\int_\Omega \mathbf{H}(\phi, t = 0)\, d\Omega}. \tag{47}$$

In the above, Ω denotes the whole computational domain. After validating the dam break problems without solid object, we proceed to demonstrate the characteristic of the LS/IB method by virtue of the four investigated dam-break problems, which all involve solid objects and undergo topological changes of the interface. In Euler framework, the gas/liquid interface will penetrate inside the solid object due to numerical errors when simulating interaction between the solid object and the interfacial flow. Several methods have been proposed to deal with this kind of problem [13,54]. Mass conservation is a essential property to be satisfied for the dam break flows in the present work. Therefore, this issue in simulating interaction between solid object and interfacial flow will be left to future studies. In this study we also

Table 1
The six calculations performed in different grids and time-step sizes.

Section	Computational domain	Grids	Time-step size Δt
6.2	5×1.25	300×75	$\Delta t = 0.005 \Delta x$
6.3	10×2	600×120	$\Delta t = 0.005 \Delta x$
6.4	4×2.4	400×240	$\Delta t = 0.002 \Delta x$
6.5	$3.2 \times 1 \times 1$	$256 \times 80 \times 80$	$\Delta t = 0.01 \Delta x$
6.6	$1.6 \times 0.6 \times 0.6$	$200 \times 75 \times 75$	$\Delta t = 0.01 \Delta x$
6.7	$16 \times 5 \times 7$	$208 \times 65 \times 91$	$\Delta t = 0.005 \Delta x$

measure the mass

$$\mathbf{M}_{\Omega_1} = \frac{\int_{\Omega_1} \mathbf{H}(\phi, t)\, d\Omega_1}{\int_{\Omega_1} \mathbf{H}(\phi, t = 0)\, d\Omega_1}. \tag{48}$$

In Eq. (48), we define $\Omega_1 \equiv \Omega \setminus \Omega_{solid}$, and Ω_{solid} is the solid region. Table 1 shows the number of uniform grids and the time-step size used in the following six dam-break flow problems.

6.1. One dimensional advection problem

The one-dimensional linear equation $\phi_t + c\phi_x = 0$ with $c = 1$ is considered subject to the following initial condition [55]

$$\phi(x) = \begin{cases} \exp\left(-\log(2)\dfrac{(x+7)^2}{0.0009}\right) & ; & -0.8 \leq x \leq -0.6 \\ 1 & ; & -0.4 \leq x \leq -0.2 \\ 1 - |10(x - 0.1)| & ; & 0 \leq x \leq 0.2 \\ \dfrac{1 - 100(x - 0.5)^2}{2}; & ; & 0.4 \leq x \leq 0.6 \\ 0 & ; & \text{otherwise.} \end{cases} \tag{49}$$

This initial conditions consist of the shapes of exponential wave, discontinuous square wave, triangular wave, and parabolic wave. The periodic boundary condition is assumed in this study. The numerical results are shown at $t = 2.0$ in Fig. 2 with the domain $[-1, 1]$ being divided into 200 uniform grids. The time step is chosen to be $\Delta t = 0.05 \Delta x$. The predicted kinks near the root of discontinuous square wave is inevitable because both UCCD and CCD schemes are not non-oscillatory schemes. However, one can see that the UCCD scheme shows less numerical oscillation than the CCD scheme in the case of the exponential wave. The reason is that the upwind-type combined compact difference scheme has an inherent artificial viscosity and, thus, can eliminate numerical oscillations.

6.2. Dam break flow on a dry bed

The lock of water was released to flow by removing a thin wall suddenly and then the water falls down freely caused by the gravity effect. The schematic of the initial condition is shown in Fig. 3. Modeling of dam break flow needs to specify the physical properties for the air and water. The water density is $\rho_L = 1000 \frac{kg}{m^3}$ and its dynamic viscosity is $\mu_L = 0.001 \frac{kg}{ms}$. The air density is $\rho_G = 1 \frac{kg}{m^3}$ and its dynamic viscosity is $\mu_G = 0.0001 \frac{kg}{ms}$. The problem under investigation is characterized by the Reynolds number $Re = \frac{\rho_L U a}{\mu_L}$. As a result, the Froude number $Fr = \frac{U}{\sqrt{ga}}$ is 1, where $U(= \sqrt{ga})$ is the characteristic velocity. No-slip conditions are specified along the horizontal and vertical walls. In Figs. 4 and 5, the numerical results predicted at two different representative Reynolds numbers, namely, 42 796 and 122 000 (i.e. $a = 0.05715$ m ($\frac{9}{4}$ inch) and $a = 0.1143$ m ($\frac{9}{2}$ inch)) in 300×75 grids are presented. We also compare the predicted front location and water column with the experiment results of Martin and Moyce [56] in Figs. 6 and 7. The water column is defined as the distance from the zero level set value to the bottom wall on the left wall (see Fig. 3).
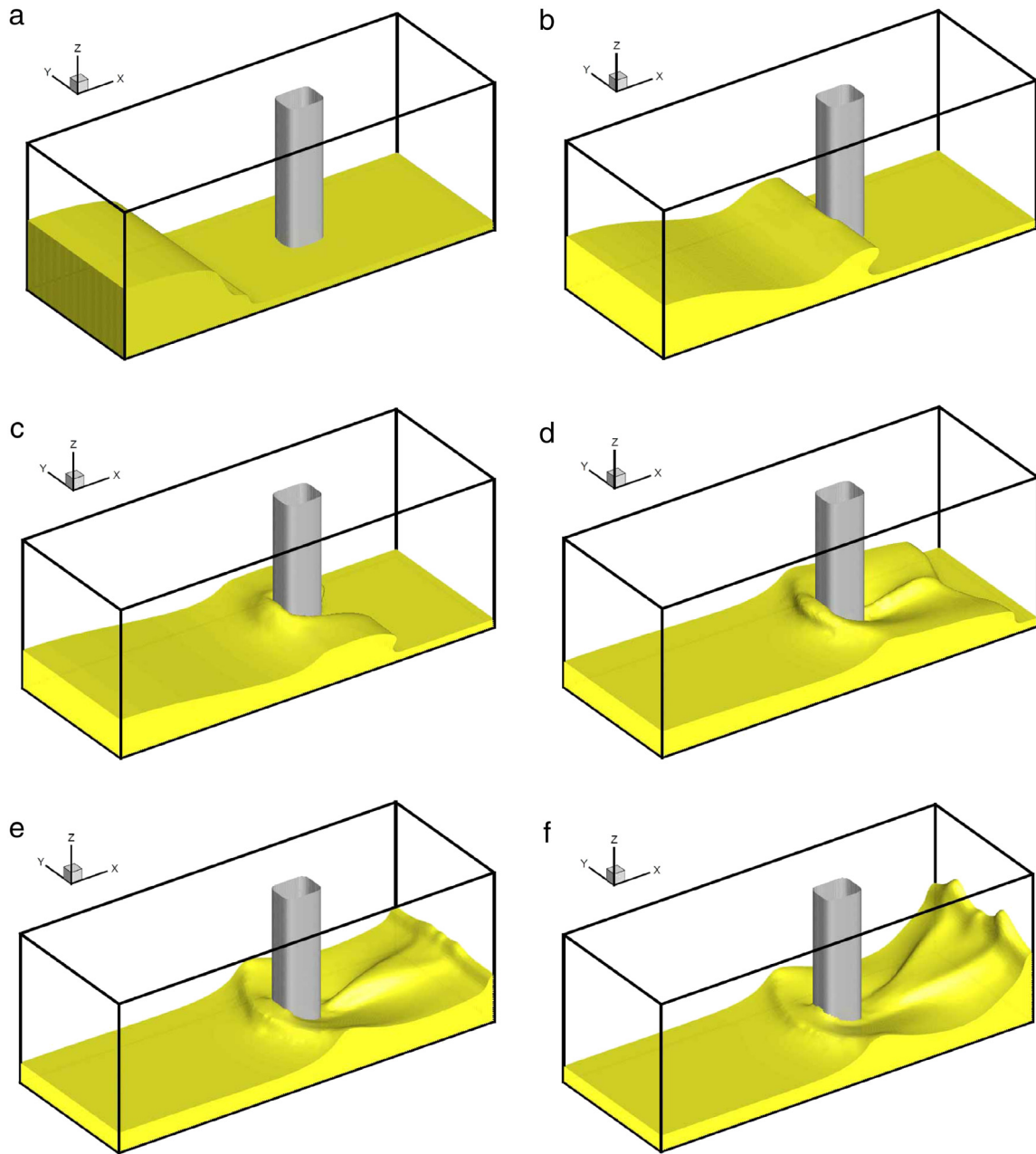
Fig. 17. The predicted time-evolving free surfaces for the 3D dam break flow against a tall structure. (a) $t = 0.18$ s; (b) $t = 0.35$ s; (c) $t = 0.50$ s; (d) $t = 0.70$ s; (e) $t = 0.85$ s; (f) $t = 1.00$ s.

It can be seen that our simulation results are in good agreement with the results of Martin and Moyce [56] predicted at different flow conditions. The Sussman's original paper [9] has been known to have its weakness in mass conservation. Therefore, we make comparison of results obtained from the present LS method with those obtained by the level set method introduced in [10]. It is also observed from Fig. 8 that the mass conservation property indeed holds well.

6.3. Dam break flow on a wet bed

The proposed level set method is also applied to simulate dam break overflow in shallow water. The simulation conditions are the same as those of Jánosi et al. [57] in order to validate the numerical model. In their experiment, the vertical baffle plate is used to enclose the water body of 0.15 m deep. In a domain of 600 × 120

grids, the predicted free surface shape in Fig. 9 is compared with experimental result. In Fig. 9(a), the moving waves are formed at the confluence of the water body and the downstream water body. In Fig. 9(c), the waves break and then merge with the downstream water, thereby resulting in a large bubble in the region of $x = 7.5 \sim x = 8.0$ at $t = 0.343$. We can see from Fig. 10 that the mass conservation deviates only slightly from the theoretical value at $t = 0.343$. However, conservative property built in the present level set method is still retained quite well.

6.4. 2D dam break flow over a rectangular obstacle

The developed LS/IB model is validated by solving the dam-break flow over a rectangular obstacle which was experimentally studied by Koshizuka et al. [58]. The tanks of area $4a \times 2.4a$ and the water column of area $a \times 2a$ are considered, where $a = 0.146$ m. A
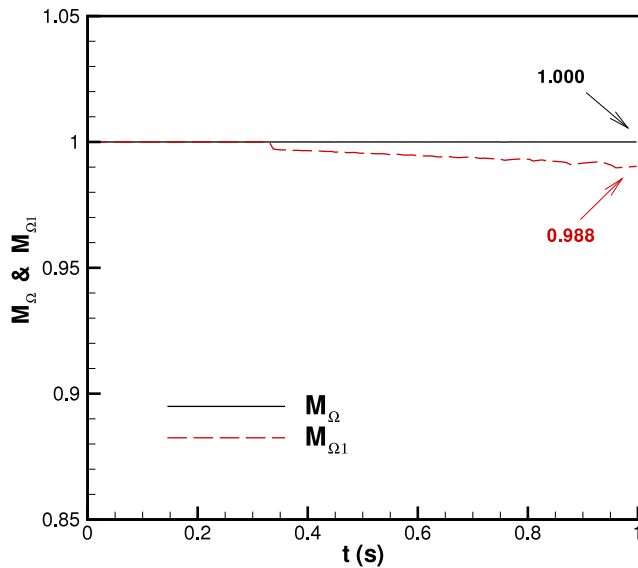
Fig. 18. The mass ratios defined in Eqs. (46) and (47) are plotted with respect to time t for the calculation carried out in $200 \times 75 \times 75$ grids.

rectangular solid obstacle placed on the bottom wall is away from the right of the water column with a distance of a. The obstacle is $2b$ in height and b in width, where $b = 2.4$ cm. The density and viscosity ratios are chosen to be $\rho_G/\rho_L = 0.001$ and $\mu_G/\mu_L = 0.01$, respectively. Three grids of the resolutions 200×120, 400×240 and 600×360 are performed for grid sensitivity studies. The solutions for mass conservation and interface can be calculated similarly for the cases with 400×240 and 600×360 grids.

Therefore, we only show the numerical results which are uniformly divided into 400×240 grids in this dam break problem. The time step chosen for this calculation is $\Delta t = 0.002 \Delta x$.

Fig. 11 shows the predicted and experimental results [58] at different times. The broken dam flow results from the removal of water gate, thereby impounding water reservoir and resulting in a flood over the rectangular bump under investigation. At a time about $t = 0.2$, water hits the rectangular bump and the wave profile changes drastically. At $t = 0.5$, when the water impacts the right wall, a bulge is formed in the numerical and experimental results. Good agreement with the numerical and experimental results given in [58] is clearly demonstrated in Fig. 11 for the free surface location. Fig. 12 shows the excellent mass preservation property for $\mathbf{M}_\Omega$. However, we see that the $\mathbf{M}_{\Omega_1}$ is not excellently conserved because a small amount of flow penetrates inside the solid object.

6.5. 3D dam break flow over a rectangle obstacle

Three dimensional dam break problem regarding the flood over a rectangle obstacle has been investigated to show if the proposed methods can be applied to simulate the formation of complex interface [59–61]. The schematic of the initial condition is shown in Fig. 13. The ρ_L and ρ_G are chosen respectively as $1000 \frac{\text{kg}}{\text{m}^3}$ and $1.0 \frac{\text{kg}}{\text{m}^3}$. The magnitudes of μ_L and μ_G are 1×10^{-3} Pa s and 1×10^{-5} Pa s. Water column with the dimension of 1.228 m $\times$ 1 m $\times$ 0.55 m hits the stationary object which has the dimension of 0.161 m $\times$ 0.41 m $\times$ 0.161 m.

In Fig. 14, the numerical result predicted in $256 \times 80 \times 80$ mesh points is presented. At $t = 1.25$, the predicted flood hits the right wall and causes the water to rebound. The predicted time-varying water heights are plotted at the observation points shown in Fig. 15 (see Fig. 13 for the locations of the water height data at the point
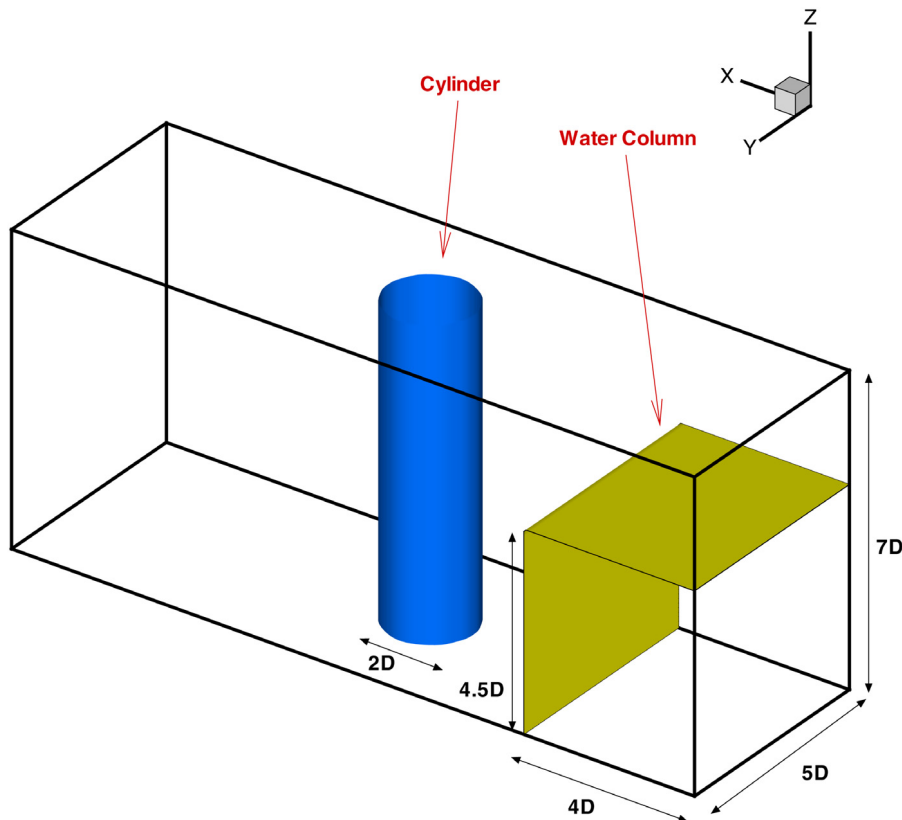

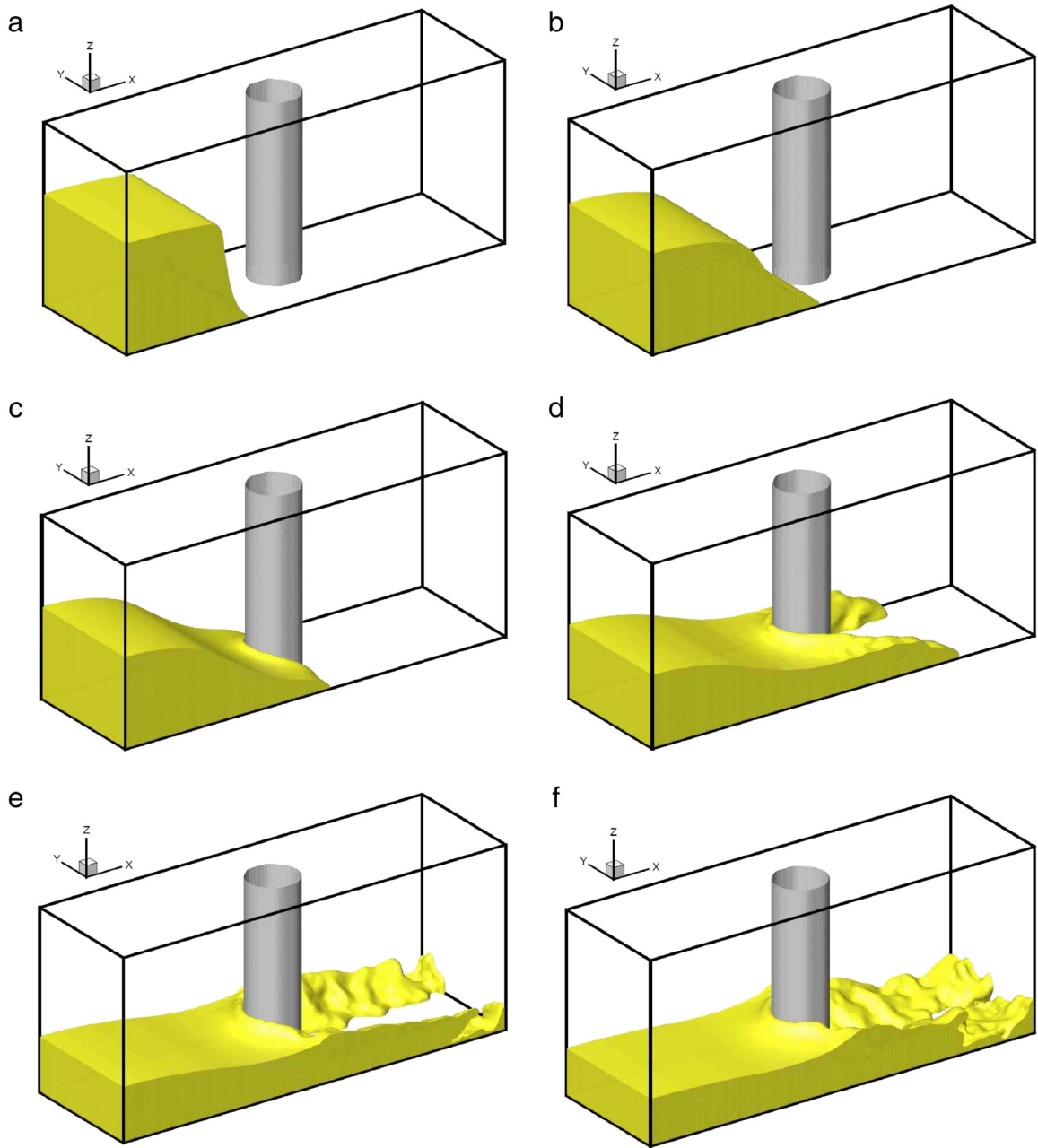**Fig. 19.** Schematic of the 3D dam break flow over a circular cylinder.

Fig. 20. The predicted time-evolving free surfaces for the 3D dam break flow over a circular cylinder at $Re = 5000$. (a) $t = 1.05$; (b) $t = 1.80$; (c) $t = 2.40$; (d) $t = 3.65$; (e) $t = 5.00$; (f) $t = 5.85$.

H_p). At the gage point H_p, water elevation is decreased in the time range of $t = 0$ s $\sim t = 2.3$ s since the water is released suddenly. When the reflected waves occurred, the progressive dam-break wave leads to a rapid increase of water level at a time about $t = 3.6$ s as Fig. 15 shows. The predicted values of $\mathbf{M}_\Omega$ and $\mathbf{M}_{\Omega_1}$ are plotted with respect to time in Fig. 16. The value of $\mathbf{M}_{\Omega_1}$ is seen to be lower by an amount less than 0.2%.

6.6. 3D dam break flow against a tall structure

The dam break flow against a tall structure, which was investigated in [62], is then simulated. Fig. 17 plots the evolution of the water elevations predicted in the domain of $200 \times 75 \times 75$ grids. The flow has hit the right wall of the tank at $t = 1.0$ and has generated a complicated flow structure. Fig. 18 shows that the mass can be well

conserved for the case investigated in the domain of $200 \times 75 \times 75$ grids.

6.7. 3D dam break flow over a circular cylinder

After validating five dam break flow problems described in the above sections, we further investigate the dam break flow over a circular cylinder. The water column is $4D \times 5D \times 4.5D$. The circular cylinder is located in the middle of the tank (or $x = 8D$, $y = 2.5D$) and has a diameter of $2D$, where D is the characteristic length. The schematic of the initial condition is shown in Fig. 19. The air–water density and viscosity ratios are specified as $\frac{\rho_G}{\rho_L} = 0.001$ and $\frac{\mu_G}{\mu_L} = 0.01$, respectively. This problem under investigation is characterized by the Reynolds number $Re(= \frac{\rho U D}{\mu}) = 5000$ and
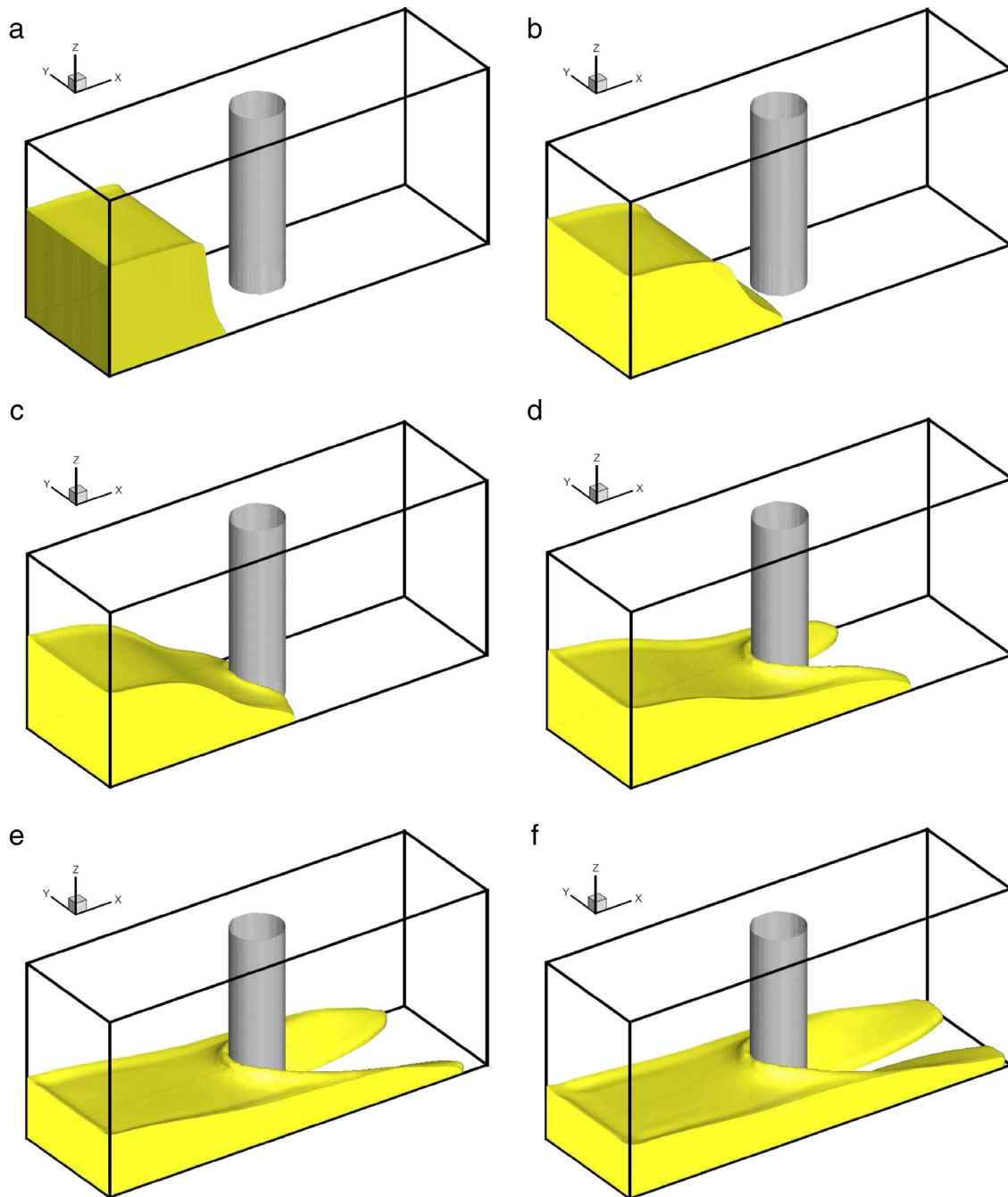
Fig. 21. The predicted time-evolving free surfaces for the 3D dam break flow over a circular cylinder at $Re = 100$. (a) $t = 1.05$; (b) $t = 1.80$; (c) $t = 2.40$; (d) $t = 3.65$; (e) $t = 5.00$; (f) $t = 5.85$.

the Froude numbers $Fr = \frac{U}{\sqrt{gD}} = 1$, where $U(= \sqrt{gD})$ is the characteristic velocity. Slip boundary condition is specified on the all walls. In Fig. 20, the free surfaces predicted in the domain of $208 \times 65 \times 91$ grids are plotted at $t = 1.05$ s, 1.80 s, 2.40 s, 5.00 s and 5.85 s. The flow has hit the right wall of the tank and has generated complex fluid structures at $t = 5.85$ s. The Reynolds number for the impact problems under investigation is high so that free-slip boundary condition is assumed. In other words, the boundary layer has a limited influence on the global flow evolution at high Reynolds numbers. This case is also investigated at $Re = 100$ and no-slip boundary condition is imposed. Fig. 21 shows the numerical results predicted in the domain of $208 \times 65 \times 91$ grids. We can see that the wave runs up to a high elevation upon impact with the obstacle block at $t = 2.40$ s. Water splashes upon hitting

the right wall at $t = 5.85$ s. The mass ratio $\mathbf{M}_\Omega$ shown in Fig. 22 is almost unchanged. $\mathbf{M}_{\Omega_1}$ is seen to decrease by an amount less than 0.2% at $Re = 100$.

7. Concluding remarks

In this paper we develop a coupled level set/immersed boundary method in collocated grids to predict dam break flow with/without solid obstacle problems. For improving interface preserving level set method, the interface is moved implicitly by the advection of level set function ϕ, which is split into three solution steps. Firstly, the symplectic Runge–Kutta temporal scheme and the upwinding combined compact difference spatial scheme featured with a minimal introduction of numerical phase error are
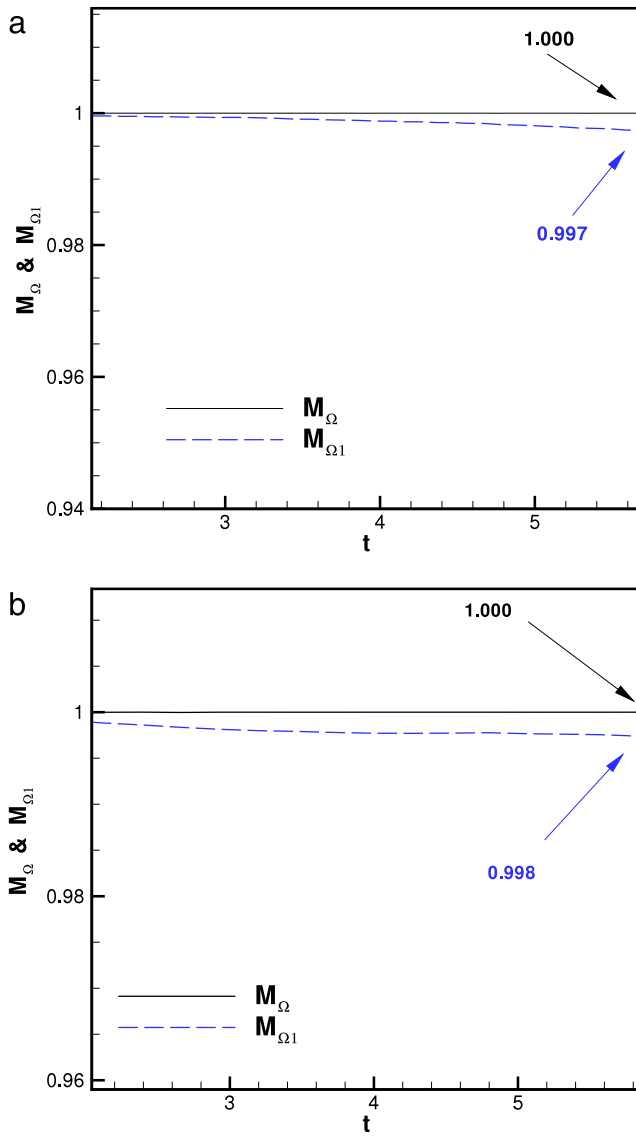
Fig. 22. The ratios defined in Eqs. (46) and (47) are plotted with respect to time t for the calculation carried out in $208 \times 65 \times 91$ grids. (a) $Re = 5000$; (b) $Re = 100$.

employed together to solve the pure advection equation. Secondly, the modified level set solution ϕ_{new} is calculated from the new smoothed Heaviside function. Finally, the correction term is added to the re-initialization equation to keep ϕ_{new} as a distance function and to conserve mass bounded by the interface. The differential-based interpolation immersed boundary method is used for the modeling of flow problems containing either a regular or an irregular solid object. This mathematical model is developed underlying the projection method to compute the incompressible Navier–Stokes solutions. Dam break flows with/without solid obstacle have been successfully simulated through the comparison of the predicted results with their corresponding experimental or other numerical results.

Acknowledgments

Appendix

The intermediate step follows the equation

$$\int_{\Omega_0} \mathbf{H}(\phi, t = 0)\, d\Omega - \int_{\Omega} \mathbf{H}(\phi, t)\, d\Omega = \mathcal{H}_{error}$$

define the average error $\mathcal{H}_{error} = \int_{\Omega} \bar{\mathcal{H}}_{error}\, d\Omega$. To show how intermediate step preserve the mass, substitute the new Heaviside function into the calculation of mass.

$$\int_{\Omega} \mathbf{H}_{new}(\phi, t)\, d\Omega = \int_{\Omega'} \mathbf{H}_{new}(\phi, t)\, d\Omega + \int_{\Omega_d} \mathbf{H}_{new}(\phi, t)\, d\Omega$$

where Ω' denotes the domain excluding interface and Ω_d denotes the interface region. Substitute Eq. (5) into the integral, obtained

$$\int_{\Omega} \mathbf{H}_{new}(\phi, t)\, d\Omega = \int_{\Omega'} \mathbf{H}_{new}(\phi, t)\, d\Omega + \int_{\Omega_d} \mathbf{H}_{new}(\phi, t)\, d\Omega$$

$$= \int_{\Omega'} \mathbf{H}(\phi, t)\, d\Omega + \int_{\Omega_d} \left[\mathbf{H}(\phi, t) + \frac{\mathcal{H}_{error}}{\mathbf{N}_{in}} \right] d\Omega$$

$$= \int_{\Omega'+\Omega_d} \mathbf{H}(\phi, t)\, d\Omega + \int_{\Omega_d} \frac{\mathcal{H}_{error}}{\mathbf{N}_{in}}\, d\Omega$$

$$= \int_{\Omega} \mathbf{H}(\phi, t)\, d\Omega + \mathcal{H}_{error} = \int_{\Omega_0} \mathbf{H}(\phi, t = 0).$$

This guarantees that intermediate steps has the better conservation of mass.

References

[1] A.J.C. Crespo, J.M. Domínguez, B.D. Rogers, M. Gómez-Gesteira, S. Longshaw, R. Canelas, R. Vacondio, A. Barreiro, O. Garcia-Feal, Comput. Phys. Comm. 187 (2015) 204–216.
[2] R. Marsooli, W. Wu, Adv. Water Resou. 70 (2014) 104–117.
[3] D. Molteni, A. Colagrossi, Comput. Phys. Comm. 180 (2009) 861–872.
[4] K.C. Ng, Y.H. Hwang, T.W.H. Sheu, Comput. Phys. Comm. 185 (2014) 2412–2426.
[5] K.C. Ng, Y.H. Hwang, T.W.H. Sheu, C.H. Yu, Comput. Phys. Comm. 196 (2015) 317–334.
[6] J. Yang, F. Stern, J. Comput. Phys. 228 (17) (2009) 6590–6616.
[7] Y. Zhang, Q. Zou, D. Greaves, D. Reeve, A. Hunt-Raby, D. Graham, P. James, X. Lv, Commun. Comput. Phys. 8 (2) (2010) 265–288.
[8] C. Zhang, N. Lin, Y. Tang, C. Zhao, Comput. Fluids 89 (2014) 214–231.
[9] M. Sussman, P. Smereka, S. Osher, J. Comput. Phys. 114 (1) (1994) 146–159.
[10] M. Sussman, E. Fatemi, SIAM J. Sci. Comput. 20 (4) (1999) 1165–1191.
[11] W. Bai, X. Liu, C.G. Koh, Ocean Eng. 97 (2015) 100–113.
[12] P. Archer, W. Bai, J. Comput. Phys. 282 (2015) 317–333.
[13] K. Yokoi, Comput. Phys. Comm. 180 (7) (2009) 1145–1149.
[14] J. Grooss, J.S. Hesthaven, Comput. Methods Appl. Mech. Engrg. 195 (25–28) (2006) 3406–3429.
[15] H. Ki, Comput. Phys. Comm. 181 (2010) 999–1007.
[16] Y.F. Yap, J.C. Chai, T.N. Wong, K.C. Toh, H.Y. Zhang, Numer. Heat Trans. B-Fund. 50 (2006) 455–472.
[17] Y. Zhang, Q. Zou, D. Greaves, Internat. J. Numer. Methods Fluids 63 (6) (2010) 651–680.
[18] M. Sussman, E.G. Puckett, J. Comput. Phys. 162 (2) (2000) 301–337.
[19] Z. Wang, J. Yang, B. Koo, F. Stern, Int. J. Multiph. Flow. 35 (3) (2009) 227–246.
[20] X. Lv, Q.P. Zou, D. Reeve, Adv. Water Resour. 34 (10) (2011) 1320–1334.
[21] K. Yokoi, J. Comput. Phys. 232 (1) (2013) 252–271.
[22] Z. Wang, J. Yang, F. Stern, J. Comput. Phys. 228 (16) (2009) 5819–5837.
[23] K. Kamran, R. Rossi, E. Oñate, Comput. Method Appl. M. 294 (2015) 1–18.
[24] T.W.H. Sheu, C.H. Yu, Commun. Comput. Phys. 11 (4) (2011) 1347–1371.
[25] C.H. Yu, T.W.H. Sheu, Commun. Comput. Phys. 18 (2015) 931–956.
[26] E. Olsson, G. Kreiss, J. Comput. Phys. 210 (1) (2005) 225–246.
[27] T.W.H. Sheu, C.H. Yu, P.H. Chiu, Int. J. Numer. Methods Fluids. 67 (2011) 109–134.
[28] R. Mittal, G. Iaccarino, Annu. Rev. Fluid Mech. 37 (2005) 239–261.
[29] C.S. Peskin, J. Comput. Phys. 10 (1972) 252–271.
[30] D. Goldstein, R. Handler, L. Sirovich, J. Comput. Phys. 105 (2) (1993) 354–366.
[31] J. Yang, E. Balaras, J. Comput. Phys. 215 (1) (2006) 12–40.
[32] L. Lee, I. Vankova, Physica D 240 (20) (2011) 1583–1592.
[33] J. Yang, F. Stern, J. Comput. Phys. 231 (15) (2012) 5029–5061.
[34] M.C. Lai, Y.H. Tseng, H. Huang, Commun. Comput. Phys. 8 (4) (2010) 735–757.

[35] M.C. Lai, C.Y. Huang, Y.M. Huang, Int. J. Numer. Anal. Mod. 8 (1) (2011) 105–117.
[36] J.J. Xu, Y. Huang, M.C. Lai, Z. Li, Commun. Comput. Phys. 15 (2) (2014) 451–469.
[37] P.H. Chiu, R.K. Lin, T.W.H. Sheu, J. Comput. Phys. 229 (12) (2010) 4476–4500.
[38] S. Tanguy, A. Berlemont, Int. J. Multiph. Flow. 31 (9) (2005) 1015–1035.
[39] S.P. van der Pijl, A. Segal, C. Vuik, P. Wesseling, Int. J. Numer. Methods Fluids. 47 (4) (2005) 339–361.
[40] P.C. Chu, C. Fan, J. Comput. Phys. 140 (2) (1998) 370–399.
[41] C.H. Yu, D. Wang, Z. He, T. Pähtz, J. Comput. Phys. 300 (2015) 92–115.
[42] D. Ghosh, J.D. Baeder, SIAM J. Sci. Comput. 34 (3) (2012) A1678–A1706.
[43] C.H. Yu, Y.G. Bhumkar, T.W.H. Sheu, J. Sci. Comput. 62 (2015) 482–516.
[44] C.K.W. Tam, J.C. Webb, J. Comput. Phys. 107 (2) (1993) 262–281.
[45] P.H. Chiu, L. Lee, T.W.H. Sheu, J. Comput. Phys. 228 (21) (2009) 8034–8052.
[46] G. Ashcroft, X. Zhang, J. Comput. Phys. 190 (2) (2003) 459–477.
[47] W. Oevel, M. Sofroniou, Symplectic Runge–Kutta schemes II: Classification of symmetric method, Univ. of Paderborn, Germany, Preprint, 1997.
[48] G.S. Jiang, D. Peng, SIAM J. Sci. Comput. 21 (6) (2000) 2126–2143.
[49] C.W. Shu, S. Osher, J. Comput. Phys. 77 (2) (1988) 439–471.
[50] T.D. Aslam, J. Comput. Phys. 193 (1) (2004) 349–355.
[51] A.J. Chorin, Math. Comp. 22 (104) (1968) 745–762.
[52] J.B. Bell, P. Colella, H.M. Glaz, J. Comput. Phys. 85 (1989) 257–283.
[53] J.B. Bell, D.L. Marcus, J. Comput. Phys. 101 (1992) 334–348.
[54] H.K. Zhao, T. Chan, B. Merriman, S. Osher, J. Comput. Phys. 127 (1996) 179–195.
[55] G.-S. Jiang, C.-W. Shu, J. Comput. Phys. 126 (1996) 202–228.
[56] J.C. Martin, W.J. Moyce, Philos. Trans. R. Soc. Lond. Ser. A Math. Phys. Eng. Sci. 244 (882) (1952) 325–334.
[57] I.M. J'anosi, D. Jan, K.G. Szabó, T. Tél, Exp. Fluids 37 (2004) 219–229.
[58] S. Koshizuka, Comput. Fluid Dyn. J. 4 (1995) 29–46.
[59] C.E. Kees, I. Akkerman, M.W. Farthing, Y. Bazilevs, J. Comput. Phys. 230 (12) (2011) 4536–4558.
[60] X. Lv, Q.P. Zou, D.E. Reeve, Y. Zhao, Commun. Comput. Phys. 11 (1) (2012) 215–248.
[61] K.M.T. Kleefsman, G. Fekken, A.E.P. Veldman, B. Iwanowski, B. Buchner, J. Comput. Phys. 206 (2005) 363–393.
[62] S. Marrone, M. Antuono, A. Colagrossi, G. Colicchio, D.L. Touzé, G. Graziani, Comput. Methods Appl. Mech. Engrg. 200 (2011) 1526–1542.